J. Fluid Mech., page 1 of 31
doi:10.1017/S0022112009008027

Flow organization in two-dimensional non-Oberbeck–Boussinesq Rayleigh–Bénard convection in water

KAZUYASU SUGIYAMA[1]†, ENRICO CALZAVARINI[1]‡, SIEGFRIED GROSSMANN[2]‖ AND DETLEF LOHSE[1]¶

[1]Physics of Fluids Group, Department of Applied Physics, J. M. Burgers Centre for Fluid Dynamics, and Impact-, MESA- and BMTI-Institutes, University of Twente, PO Box 217, 7500 AE Enschede, The Netherlands

[2]Fachbereich Physik der Philipps-Universitaet, Renthof 6, D-35032 Marburg, Germany

(Received 19 December 2008; revised 5 May 2009; accepted 6 May 2009)

Non-Oberbeck–Boussinesq (NOB) effects on the flow organization in two-dimensional Rayleigh–Bénard turbulence are numerically analysed. The working fluid is water. We focus on the temperature profiles, the centre temperature, the Nusselt number and on the analysis of the velocity field. Several velocity amplitudes (or Reynolds numbers) and several kinetic profiles are introduced and studied; these together describe the various features of the rather complex flow organization. The results are presented both as functions of the Rayleigh number Ra (with Ra up to 10^8) for fixed temperature difference Δ between top and bottom plates and as functions of Δ ('non-Oberbeck–Boussinesqness') for fixed Ra with Δ up to 60 K. All results are consistent with the available experimental NOB data for the centre temperature T_c and the Nusselt number ratio Nu_{NOB}/Nu_{OB} (the label OB meaning that the Oberbeck–Boussinesq conditions are valid). For the temperature profiles we find – due to plume emission from the boundary layers – increasing deviations from the extended Prandtl–Blasius boundary layer theory presented in Ahlers *et al.* (*J. Fluid Mech.*, vol. 569, 2006, p. 409) with increasing Ra, while the centre temperature itself is surprisingly well predicted by that theory. For given non-Oberbeck–Boussinesqness Δ, both the centre temperature T_c and the Nusselt number ratio Nu_{NOB}/Nu_{OB} only weakly depend on Ra in the Ra range considered here.

Beyond $Ra \approx 10^6$ the flow consists of a large diagonal centre convection roll and two smaller rolls in the upper and lower corners, respectively ('corner flows'). Also in the NOB case the centre convection roll is still characterized by only one velocity scale. In contrast, the top and bottom corner flows are then of different strengths, the bottom one being a factor 1.3 faster (for $\Delta = 40$ K) than the top one, due to the lower viscosity in the hotter bottom boundary layer. Under NOB conditions the enhanced lower corner flow as well as the enhanced centre roll lead to an enhancement of the volume averaged energy based Reynolds number $Re^E = \langle \frac{1}{2}\boldsymbol{u}^2 \rangle^{1/2} L/\nu$ of about 4 % to 5 % for $\Delta = 60$ K. Moreover, we find $Re^E_{NOB}/Re^E_{OB} \approx (\beta(T_c)/\beta(T_m))^{1/2}$, with β the thermal expansion coefficient and T_m the arithmetic mean temperature between

† Present address: Department of Mechanical Engineering, School of Engineering, The University of Tokyo, 7-3-1 Hongo, Bunkyo-ku, Tokyo 113-8656, Japan. Email: sugiyama@fel.t.u-tokyo.ac.jp

‡ Present address: Laboratoire de Physique de École Normale Supérieure de Lyon and CNRS, 46 Allée d'Italie, 69007 Lyon, France. Email: enrico.calzavarini@ens-lyon.fr

‖ Email: grossmann@physik.uni-marburg.de

¶ Email address for correspondence: d.lohse@utwente.nl

top and bottom plate temperatures. This corresponds to the ratio of the free fall velocities at the respective temperatures. By artificially switching off the temperature dependence of β in the numerics, the NOB modifications of Re^E is less than 1 % even at $\Delta = 60\,\mathrm{K}$, revealing the temperature dependence of the thermal expansion coefficient as the main origin of the NOB effects on the global Reynolds number in water.

1. Introduction

Rayleigh–Bénard (RB) convection in the Oberbeck–Boussinesq (OB) approximation (Oberbeck 1879; Boussinesq 1903) is rather a mathematical concept than physical reality. On the one hand it is driven by a temperature difference $\Delta = T_b - T_t$ between the bottom and top plates, whose distance in height is L; on the other hand, the temperature dependences of the material properties such as the kinematic viscosity ν, the thermal diffusivity κ, the heat conductivity Λ, the isobaric specific heat capacity c_p and the isobaric thermal expansion coefficient β are all ignored in the OB approximation apart from that of the density ρ, which is assumed to vary linearly with T:

$$\rho(T) \approx \rho_m(1 - \beta_m(T - T_m)). \tag{1.1}$$

Here, $T_m = (T_t + T_b)/2$ is the arithmetic mean value of the warmer bottom plate temperature T_b and the colder top plate temperature T_t, and ρ_m and β_m denote the density and the thermal expansion coefficient at the mean temperature T_m, respectively. Fortunately, the OB approximation is rather good, if the material properties depend on temperature only weakly or if the temperature difference Δ between the bottom and top plates is kept small enough. However, if either the material properties are strongly temperature dependent (as, for example, the viscosity of glycerol in some temperature regimes) or if the temperature difference between bottom and top plates is chosen to be large in order to achieve larger Rayleigh numbers, the deviations from the OB approximation are expected to become relevant. The consequences of these deviations are called non-Oberbeck–Boussinesq (NOB) effects (Ahlers *et al.* 2006; Ahlers, Grossmann & Lohse 2009). To what extent they affect the Nusselt number and whether they possibly could account for the differences between the Oregon and the Grenoble data is an ongoing controversy (Chavanne *et al.* 1997; Ashkenazi & Steinberg 1999; Niemela *et al.* 2000, 2001; Chavanne *et al.* 2001; Roche *et al.* 2001, 2002; Niemela & Sreenivasan 2003).

The signatures of NOB effects studied in this article are (i) a deviation of the centre (or bulk) temperature T_c from the arithmetic mean temperature T_m, (ii) a modified z profile of the area averaged temperature, which develops a bottom–top asymmetry, (iii) different thermal boundary layer thicknesses $\lambda_b \neq \lambda_t$ at the bottom and top together with different temperature drops $\Delta_b \neq \Delta_t$ across these boundary layers (BLs), (iv) a modification of the Nusselt number, best expressed by the ratio Nu_{NOB}/Nu_{OB} and (v) a bottom–top symmetry broken flow structure, in particular possibly different amplitudes $U_b \neq U_t$ of the plate-parallel winds near the bottom and top plates meaning different Reynolds numbers $Re_{b,t} = U_{b,t}/(\nu L^{-1})$.

Some of the NOB deviations will turn out to be tiny, as the NOB effects from the top and from the bottom BLs partly compensate each other. Nevertheless, they are important to understand, in order to judge on the validity and quality of the

OB approximation in various high-Rayleigh-number experiments. Moreover, it is interesting from a fundamental point of view, in order to understand how NOB effects break the top–bottom symmetry of the purely OB–RB convection.

The deviation $T_c - T_m$ of the centre temperature from the arithmetic mean temperature and the corresponding differences between the temperature drops Δ_t and Δ_b over the thermal BLs presumably is the experimentally most explored NOB effect, namely for water by Wu & Libchaber (1991) and by Ahlers *et al.* (2006, 2007, 2008); Ahlers, Grossmann & Lohse (2009). While for water even for $\Delta = 50\,\mathrm{K}$ (leading to roughly a factor two variation of the viscosity of the bottom and top liquid layers) the deviation $T_c - T_m$ is only at most 2 K, for glycerol this deviation can be as large as 8 K (Zhang, Childress & Libchaber 1997; Sugiyama *et al.* 2007)

To theoretically account for these deviations, in Ahlers *et al.* (2006) the Prandtl–Blasius boundary layer (BL) theory was extended to the NOB case, giving surprisingly good agreement with the experimental centre temperatures T_c for water. Also for ethane gas, which is compressible, the BL theory – extended to compressible fluid flow – can describe the measured centre temperature data rather satisfactorily, as presented in Ahlers *et al.* (2007). But as was shown in Ahlers *et al.* (2008), the T-dependence of the buoyancy caused by thermal expansion $\beta = \beta(T)$ is the dominant cause of the observed NOB effects, in particular the characteristic differences between the more gas-like and the more liquid-like ethane on the two sides of the critical isochore.

The success of the Prandtl–Blasius BL theory in the context of NOB convection is remarkable for at least two reasons: first, the boundary layer theory deals with semi-infinite plates, while experiments are done in finite aspect ratio containers, mainly for $\Gamma = 1$; second, and more importantly, the Prandtl–Blasius BL theory completely ignores the plume separations and the corresponding time dependence of the boundary layer flow. Although the shear Reynolds numbers in the BLs are not yet very large in RB flow (for $Pr = 1$ the transitional shear Reynolds number $Re_\star^S \approx 420$, which indicates the range of turbulence transition, is only reached near $Ra \approx 10^{14}$, see Grossmann & Lohse 2002), the plumes (and thus the time dependence of the BL flow) play a significant role in the heat transfer (Ciliberto, Cioni & Laroche 1996; Ciliberto & Laroche 1999) and perhaps also for the bulk temperature T_c. Plumes are not included in the classical BL theory because that does not take notice of the buoyant forcing in the Prandtl approximation of the hydrodynamic equations of motion. Neither the thermal expansion coefficient β itself is addressed nor is its temperature dependence taken into account, which in reality is considerable. For water at $T_m = 40\,^\circ\mathrm{C}$ and $\Delta = 40\,\mathrm{K}$ there is nearly a factor of 2 between the respective values β_t and β_b at the top and bottom plates. Technically speaking, the BL theory misses β since buoyancy shows up in the equation of the vertical velocity field u_z; and this equation enters into the Prandtl approximation only to derive the height independence of the pressure, which in RB anyhow does not play a role. The numerical simulations presented in this paper will quantitatively show that buoyancy and plumes indeed affect the temperature BL profiles.

There are two further assumptions of the extended BL theory developed in Ahlers *et al.* (2006) which need to be tested: first, the extended BL theory assumes that the large scale wind velocity is the same close to the top and the bottom plate, i.e. $U_t = U_b$ or $Re_t = Re_b \equiv Re_{NOB}$. We will show in this paper that there are several relevant velocity amplitudes, most of which break the top–bottom symmetry. Only the main central roll has the same amplitude near the bottom as well as the top boundary layers. Second, within the BL theory the ratios Nu_{NOB}/Nu_{OB} and Re_{NOB}/Re_{OB} cannot be

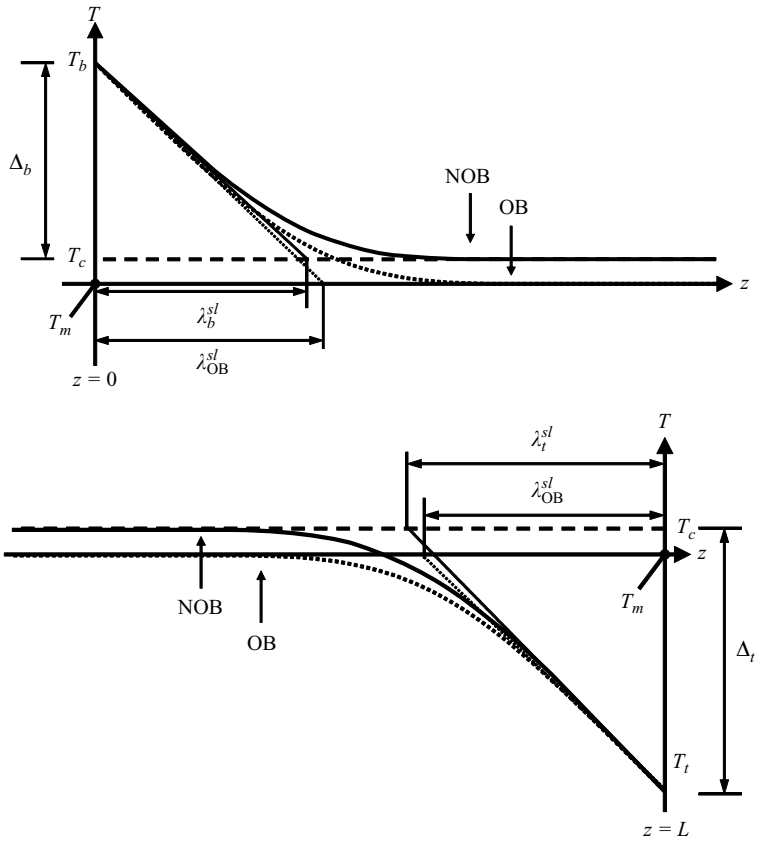

FIGURE 1. Notations and sketch of the time and surface averaged temperature profiles versus height z in the OB and NOB cases, respectively. The height of the cell is L (not shown). The temperatures at the top ($z = L$) and the bottom ($z = 0$) plates are T_t and T_b, their arithmetic mean is $T_m = (T_t + T_b)/2$. The thermal BL thicknesses based on the temperature slopes at the plates are called $\lambda_{t,b}^{sl}$. The respective temperature drops are Δ_t and Δ_b. The time averaged temperature in the bulk (or centre) is T_c. For water as the working fluid, this centre temperature T_c is larger than T_m. While $\lambda_b^{sl} = \lambda_t^{sl}$ in the OB case, under NOB conditions the bottom BL is thinner than the top one, $\lambda_b^{sl} < \lambda_t^{sl}$. The fluid properties such as ν, κ and β carry the same index as the temperature at which they are considered, e.g. $\nu_t = \nu(T_t)$ for the kinematic viscosity at the top plate, and so on.

calculated at all, in contrast to T_c. These quantities can only be obtained by additional input from experiment, namely by employing the experimental information on the ratio $F_\lambda := 2\lambda_{OB}^{sl}/(\lambda_t^{sl} + \lambda_b^{sl})$. Here λ_t^{sl} and λ_b^{sl} are the top and bottom thermal BL thicknesses, defined via the temperature slopes at the plates in (4.1) and sketched in figure 1. In Ahlers *et al.* (2006) we have calculated F_λ from the measured Nusselt number and the calculated centre temperature. Its value T_c determines the ratio $F_\Delta := (\kappa_t \Delta_t + \kappa_b \Delta_b)/(\kappa_m \Delta)$. The exact relation holds (even for compressible flow) (the notation used in (1.2) is explained in the caption of figure 1)

$$\frac{Nu_{NOB}}{Nu_{OB}} = \frac{2\lambda_{OB}^{sl}}{\lambda_t^{sl} + \lambda_b^{sl}} \cdot \frac{\kappa_t \Delta_t + \kappa_b \Delta_b}{\kappa_m \Delta} =: F_\lambda \cdot F_\Delta. \tag{1.2}$$

Nu_{NOB} is the actual heat flux with all material parameters taken at their respective real temperature values. The label OB means that all fluid properties are taken as temperature independent constants, evaluated at the arithmetic mean temperature T_m.

Remarkably, for the analysed case of water at $T_m = 40\,^{\circ}\mathrm{C}$ (Ahlers *et al.* 2006) the experimental data are consistent with $F_\lambda = 1$. But as was shown in Calzavarini, Grossmann & Lohse (2007) by numerical simulations it is $F_\lambda \neq 1$ for RB convection in glycerol under NOB conditions, at least up to $Ra = 10^8$. However, in glycerol due to the large Prandtl number $Pr \approx 2500$, a large-scale convection roll did not yet develop and it could be that $F_\lambda = 1$ is connected with the existence of such a roll. The numerical simulations presented in this paper will unambiguously show that $F_\lambda = 1$ does *not* hold in general. This property thus is coincidental for water due to the specific temperature dependences of its material properties around $40\,^{\circ}\mathrm{C}$.

The question of modifications of the Reynolds number(s) through NOB effects is intimately related to the flow organization. In recent years there was considerable progress in our insight into the flow structure, thanks to numerical simulations (Verzicco & Camussi 2003; Schmalzl, Breuer & Hansen 2004; Amati *et al.* 2005; Stringano & Verzicco 2006; Shishkina & Wagner 2008; Stevens, Verzicco & Lohse 2009), to particle image velocimetry (PIV) measurements (Xia, Sun & Zhou 2003; Qiu *et al.* 2004; Xi, Lam & Xia 2004; Sun, Xi & Xia 2005*a*; Sun, Xia & Tong 2005*b*) and to velocity correlation measurements (Brown, Funfschilling & Ahlers 2007). These papers revealed that there are various feasible possibilities to define flow amplitudes and that these differently defined amplitudes and the corresponding Reynolds numbers have different scaling behaviour with Ra. Our numerical simulations have fully confirmed and detailed this view. We will show that NOB conditions influence the flow structure near top and bottom differently and modify the various Reynolds numbers correspondingly. NOB conditions have the largest impact on the convective flow in one top and one bottom corner of the cell, where macroscopically visible secondary rolls develop. We will also show that the NOB modification of the global, volume and time averaged, energy based Reynolds number $Re^E = \langle \frac{1}{2}\boldsymbol{u}^2 \rangle_{V,\tau}^{1/2}/(\nu L^{-1})$ is consistent with attributing it mainly to the change of the thermal expansion coefficient β in the bulk. More specifically, we find $Re^E_{NOB}/Re^E_{OB} \approx (\beta(T_c)/\beta(T_m))^{1/2}$, a finding clearly not describable within the extended Prandtl–Blasius BL theory.

In this paper we focus on water ($Pr = 4.4$). Nevertheless, the parameter space is considerable. Next to Ra the crucial parameter is the NOBness Δ. For comparison we perform numerical simulations for fluids with non-physical temperature dependences of their material properties in order to clarify the origin of certain observations.

As the numerical effort is so large for three-dimensional simulations we restrict ourselves to two-dimensional simulations. One may worry on whether two-dimensional simulations are sufficient to reflect the dynamics of three-dimensional RB convection. For heat flow under OB conditions this point has been analysed in detail by Schmalzl *et al.* (2004) and earlier by DeLuca *et al.* (1990), Werne *et al.* (1991) and Werne (1993). Recently, Johnston & Doering (2009) compared two-dimensional Rayleigh–Bénard convection with constant temperature and with constant flux boundary conditions. Schmalzl *et al.* (2004)'s conclusion is that for $Pr \gtrsim 1$ various properties observed in numerical three-dimensional convection (and thus also in experiment) are well reflected in the two-dimensional simulations. This in particular holds for the BL profiles and for the Nusselt numbers. Since one focus of this paper is on the difference between OB and NOB convection, the restriction to two-dimensional simulations might be even less severe, as NOB deviations occur in both cases and the differences between two-dimensional and three-dimensional

simulations might cancel out in quantities such as $(T_c - T_m)/T_m$, Nu_{NOB}/Nu_{OB}, or Re_{NOB}/Re_{OB}. We also note that for a comparison with the Prandtl–Blasius BL theory two-dimensional simulations are in fact more appropriate than three-dimensional simulations, as the BL theory is two-dimensional per construction.

The paper is organized as follows: in § 2 we will explain, justify and verify the numerical method; § 3 is devoted to our results on the mean temperature profiles and the related shifts of the centre temperatures; § 4 addresses the NOB effects on the Nusselt number. The main section is § 5 where we first analyse the flow structure for the OB case and then its modifications through NOB effects. Several feasible measures for the wind amplitudes of the complex flow structure will be introduced. Section 6 contains the conclusions.

2. Definitions, governing equations and numerical method

The equations governing non-Oberbeck–Boussinesq convection in incompressible liquids are the incompressibility condition

$$\partial_i u_i = 0, \tag{2.1}$$

the Navier–Stokes equation

$$\rho_m(\partial_t u_i + u_j \partial_j u_i) = -\partial_i p + \partial_j(\eta(\partial_j u_i + \partial_i u_j)) + \rho_m g \left(1 - \frac{\rho}{\rho_m}\right) \delta_{i3}, \tag{2.2}$$

and the heat-transfer equation

$$\rho_m c_{p,m}(\partial_t T + u_j \partial_j T) = \partial_j(\Lambda \partial_j T). \tag{2.3}$$

The dynamic viscosity $\eta(T)$ and the heat conductivity $\Lambda(T)$ are both temperature and thus space dependent. The isobaric specific heat capacity c_p and the density ρ are assumed as constants and their values $c_{p,m}$ and ρ_m are fixed at the temperature T_m, except in the buoyancy term, where the full nonlinear temperature dependence of $\rho(T)$ is implemented. For water, which we here consider as the working fluid, density as well as specific heat are indeed constant with temperature to a very good approximation. The experimentally known temperature dependences of η, Λ and ρ (in the buoyancy term) together with the values of the parameters ρ_m and $c_{p,m}$ for water are given in the appendix of Ahlers *et al.* (2006) and, for better reference, are reported in table 1 in the form implemented in the present direct numerical simulations (DNS).

We deal with a wall-bounded system with an aspect ratio fixed at $\Gamma = 1$. The velocity boundary conditions accompanying the dynamical equations are $u_i = 0$ at the top and bottom plates $z = L$ and $z = 0$ as well as on the sidewalls $x = 0$, $x = L$. The temperature boundary conditions are $T_b - T_t = \Delta$ for the temperature drop across the whole cell of height L. At the sidewalls ($x = 0,\ x = L$) heat-insulating conditions are employed, $\partial_x T|_{x=0,L} = 0$. The cell is considered to be two-dimensional, i.e. there is no y-dependence. The Rayleigh number is defined with the material parameters taken at the mean temperature T_m,

$$Ra = \frac{\beta_m g L^3 \Delta}{\nu_m \kappa_m}. \tag{2.4}$$

We vary the Rayleigh number in DNS by varying the height L of the box, while the non-Oberbeck–Boussinesqness is changed by varying the temperature drop Δ. Note that in (2.2) the full temperature dependence of the density in the buoyancy term is taken into account, rather than employing the linear approximation (1.1) only. Still the Rayleigh number is defined with the coefficient of the linear expansion of the density

n	ν A_n	κ B_n	$g(1-\rho/\rho_m)$ C_n
0	$6.6945204\cdot10^{-7}$ $(\mathrm{m^2\,s^{-1}})$	$1.5222630\cdot10^{-7}$ $(\mathrm{m^2\,s^{-1}})$	0 $(\mathrm{m^2\,s^{-1}})$
1	$-1.215394\cdot10^{-8}$ $(\mathrm{m^2\,s^{-1}\,K^{-1}})$	$3.347639\cdot10^{-10}$ $(\mathrm{m^2\,s^{-1}\,K^{-1}})$	$3.7576156\cdot10^{-3}$ $(\mathrm{m\,s^{-2}\,K^{-1}})$
2	$1.737730\cdot10^{-10}$ $(\mathrm{m^2\,s^{-1}\,K^{-2}})$	$-2.702875\cdot10^{-12}$ $(\mathrm{m^2\,s^{-1}\,K^{-2}})$	$3.900878\cdot10^{-5}$ $(\mathrm{m\,s^{-2}\,K^{-2}})$
3	$-2.48455\cdot10^{-12}$ $(\mathrm{m^2\,s^{-1}\,K^{-3}})$	0	$-1.811623\cdot10^{-7}$ $(\mathrm{m\,s^{-2}\,K^{-3}})$
4	$3.55232\cdot10^{-14}$ $(\mathrm{m^2\,s^{-1}\,K^{-4}})$	0	0
5	$-5.0790\cdot10^{-16}$ $(\mathrm{m^2\,s^{-1}\,K^{-5}})$	0	0

TABLE 1. Expansion coefficients of material properties of water around the temperature $T_m = 40\,^\circ\mathrm{C}$ adapted from Ahlers *et al.* (2006). The kinematic viscosity, the thermal diffusivity and buoyancy are written in a polynomial form as $\nu(T) \equiv \eta(T)/\rho_m = \sum_{n=0} A_n (T - T_m)^n$, $\kappa(T) \equiv \Lambda(T)/(\rho_m c_{p,m}) = \sum_{n=0} B_n (T - T_m)^n$ and $g(1-\rho(T)/\rho_m) = \sum_{n=0} C_n (T - T_m)^n$, respectively. Using the leading coefficient $C_1 (= g\beta_m)$ for the buoyancy force, we can write the Rayleigh number defined in (2.4) as $Ra = C_1 L^3 \Delta/(\nu_m \kappa_m)$, where $\nu_m = \eta(T_m)/\rho_m$ and $\kappa_m = \Lambda(T_m)/(\rho_m c_{pm})$, which coincides with the usual OB definition. Note that in Ahlers *et al.* (2006) we instead directly expanded $\nu(T) = \eta(T)/\rho(T)$ (and correspondingly for $\kappa(T)$) around T_m, leading to slightly different coefficients.

with respect to temperature, taken at the mean temperature, $\beta_m = -\rho_m^{-1} \partial\rho/\partial T|_{T_m}$, cf. table 1. The Prandtl number $Pr = \nu_m/\kappa_m$ is also defined in terms of the material parameters at the arithmetic mean temperature.

Equations (2.1)–(2.3) are solved on a two-dimensional domain with gravity pointing in negative z direction. To discretize the Navier–Stokes and heat transfer equations, we employ a finite difference scheme (see e.g. Peyret & Taylor 1983; Ferziger & Perić 1996). The space derivatives are approximated by the fourth-order central difference scheme on a staggered grid (Harlow & Welch 1965). In particular for the advection terms we employ the scheme proposed by Kajishima *et al.* (2001), which satisfies the relations $\partial_j(u_j u_i) = u_i \partial_j u_j + u_j \partial_j u_i$ and $\partial_j(u_j T) = T \partial_j u_j + u_j \partial_j T$ in a discretized form and ensures that the second moments of the velocity and temperature are highly conserved. To integrate the equations in time, we use the second-order scheme, i.e. the Adams–Bashforth method for the advection terms and the Crank–Nicolson one for the viscous, diffusive and buoyant terms (see e.g. Canuto *et al.* 1988). To complete the time marching in the momentum equation and simultaneously satisfying the solenoidal condition (2.1) of the velocity vector, we employ a simplified-marker-and-cell procedure (Amsden & Harlow 1970) by solving a Poisson equation for the pressure. The two-dimensional discretized pressure equation, which is written in the fourth-order finite difference form, is reduced into a one-dimensional problem by taking the fast fourier transform (FFT) in the x direction. The boundary condition at the sidewalls ($x = 0$ and $x = L$) is satisfied, if the relation $\partial_x \phi|_{x=0} = \partial_x \phi|_{x=L} = 0$ holds for all the quantities ϕ in the pressure equation. To impose this condition, we take a periodicity $2L$ for the FFT (i.e. $\phi(x) = \phi(2nL + x)$ with n an arbitrary integer) and introduce a fictitious domain $L < x \leqslant 2L$, in which the quantities are given by $\phi(x) = \phi(2L - x)$. We directly solve the reduced-order equation written in a heptadiagonal matrix form and then determine the pressure field by taking the inverse FFT.

We briefly comment on the temporal and spatial resolution. The time step is chosen such that the Courant–Friedrichs–Lewy (CFL) condition is fulfilled: the CFL number is 0.2 or less for all the present computations. The spatial resolution is chosen according to Grötzbach (1983) (see also Shishkina & Wagner 2008) such that the linear expansion h of a numerical grid cell obeys $h/\eta_K \leqslant \pi \min(1, Pr^{-3/4})$. For our case $Pr = 4.4$ this implies $h/\eta_K \leqslant 1.03$. Here $\eta_K = \epsilon_u^{-1/4} \nu^{3/4}$ is the Kolmogorov length

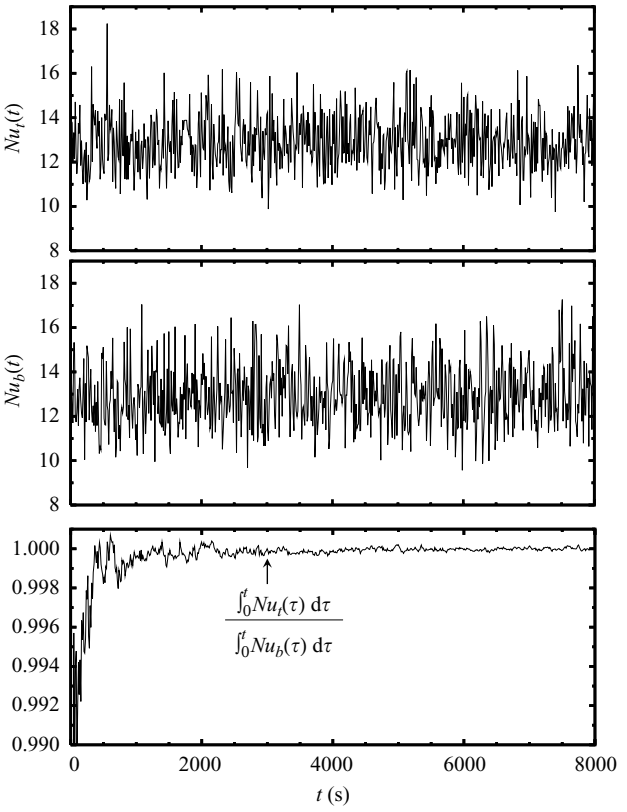

FIGURE 2. Upper two panels: temporal evolution of $Nu_t(\tau)$ and $Nu_b(\tau)$ as defined in equation (2.5), before time averaging, for $Ra = 10^7$, $\Delta = 40$ K and $L = 1.89$ cm. The total integration time $\mathscr{T}$, reported here in seconds, is of the order 10^4 integral times of the autocorrelation coefficient, $\tau_I \simeq 0.606$ s. Lowest panel: ratio of the temporally averaged Nusselt numbers $\int_0^t Nu_t(\tau)\,\mathrm{d}\tau / \int_0^t Nu_b(\tau)\,\mathrm{d}\tau$. Here the time averages at top and bottom agree up to 0.009 %. For other Ra and Δ the statistical convergence is similar with maximum relative error being 0.091 %.

scale and ϵ_u is the turbulent kinetic-energy dissipation rate. The highest value of h/η_K in our simulations is 0.653 at the highest Rayleigh number $Ra = 10^8$, obeying the Grötzbach criterion.

We have validated the numerical code by checking the instantaneous kinetic energy and entropy budget relations for $\boldsymbol{u}^2/2$ and $T^2/2$ both in the OB and NOB cases and by evaluating the correctness of the onset of convection in the OB case. The critical Rayleigh number we compute ($Ra_c = 2585.27$) is in agreement with the one computed analytically by Luijkx & Platten (1981) ($Ra_c = 2585.03$) to a precision of less than 0.01 %. We note that Ra_c is much larger than the more known $Ra_c = 1708$ for an infinite aspect ratio system, due to the presence of lateral walls.

The area averaged heat currents are calculated as functions of time τ both at the top (t) and the bottom (b) plates separately,

$$Nu_t(\tau) = \frac{-\kappa_t\ \partial_z \langle T \rangle_{A_t}(z = L, \tau)}{\kappa_m \Delta / L}\,, \qquad Nu_b(\tau) = \frac{-\kappa_b\ \partial_z \langle T \rangle_{A_b}(z = 0, \tau)}{\kappa_m \Delta / L}, \tag{2.5}$$

with $\langle \ldots \rangle_A$ denoting the averaging over the horizontal surface (actually over x only, since the system is two-dimensional) of the top and bottom plates. We find good agreement of the time averages of $Nu_t(\tau)$, $Nu_b(\tau)$ (see figure 2).

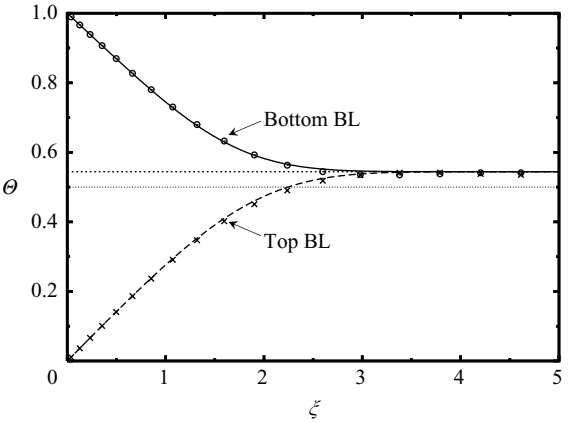

FIGURE 3. Temperature profiles $\Theta(\xi) = (\langle T \rangle_{A(\xi)} - T_t)/\Delta$ for $Ra = 10^4$ and $\Delta = 40\,\mathrm{K}$ for water at $T_m = 40\,^\circ\mathrm{C}$. The symbols indicate the results of the numerical simulation, the lines stem from the extended Prandtl–Blasius BL theory proposed in Ahlers *et al.* (2006). The numerical simulations give $\Theta(z)$. $\xi = z/l_{BL}$ is the similarity variable. In classical BL theory its scale is given by $l_{BL} = \sqrt{x\nu_m/U_{t,b}}$ with x being the distance from the plate's edge; in this figure in order to translate to $\Theta(\xi)$ we have chosen the factor l_{BL} such that the curves have the same slope at $\xi = 0$.

To quantify the statistical convergence, we make an uncertainty analysis estimating the time autocorrelations (see, for instance, Tennekes & Lumley 1972, § 6.4). For a time-dependent function $f(\tau)$, the error is evaluated as $\delta f = f_{rms}\sqrt{2\tau_I/\mathscr{T}}$; here f_{rms} is the root mean square of f, τ_I the integral time obtained from the autocorrelation coefficient of f and $\mathscr{T}$ the total simulation time under statistically steady conditions, i.e. after a transient time τ_0. Considering the error propagation, we evaluate the errors of $F_\lambda \cdot F_\Delta$, of F_λ and of F_Δ at 95 % confidence level as, respectively,

$$\begin{aligned}
\delta(F_\lambda F_\Delta) &= \frac{Nu_{NOB}}{Nu_{OB}}\sqrt{\left(\frac{\delta(Nu_{NOB})}{Nu_{NOB}}\right)^2 + \left(\frac{\delta(Nu_{OB})}{Nu_{OB}}\right)^2}, \\
\delta(F_\lambda) &= F_\lambda\sqrt{\left(\frac{\delta(Nu_{NOB})}{Nu_{NOB}}\right)^2 + \left(\frac{\delta(Nu_{OB})}{Nu_{OB}}\right)^2 + \left(\frac{\delta(F_\Delta)}{F_\Delta}\right)^2}, \\
\delta(F_\Delta) &= \left|\frac{\kappa_b - \kappa_t}{\kappa_m \Delta}\right| \delta(T_c),
\end{aligned} \tag{2.6}$$

which will be indicated by the error bars in the plots.

3. Mean temperature profiles and centre temperature

We will first focus on the water case with $T_m = 40\,^\circ\mathrm{C}$, corresponding to the experiments of Ahlers *et al.* (2006). In figures 3 and 4 the mean temperature profiles, averaged over the full width $0 \leqslant x \leqslant L$ of the cell, are shown for $Ra = 10^4$ and $Ra = 10^8$, respectively and compared with the extended Prandtl–Blasius BL theory developed in Ahlers *et al.* (2006) (the specific procedure adopted for the comparison is detailed in the caption of figure 3).

For $Ra = 10^4$ the agreement between numerical data and the time independent extended BL theory is excellent, both for the profiles and for the centre temperature.

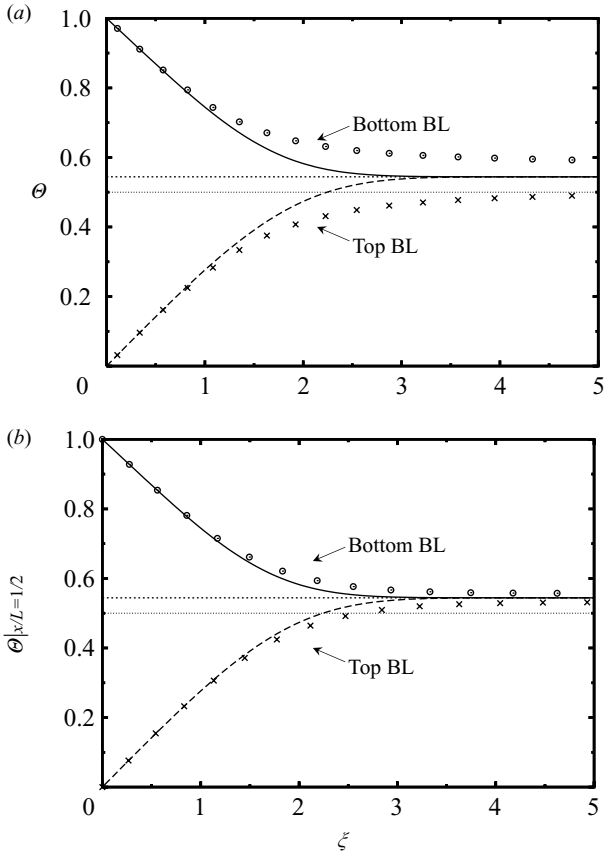

FIGURE 4. Temperature profiles at $Ra = 10^8$ with $\Delta = 40\,\mathrm{K}$ and $T_m = 40\,^\circ\mathrm{C}$ in water. (*a*) Horizontally area averaged temperature profiles as in figure 3. Though the centre temperature T_c is well described by the extended Prandtl–Blasius BL theory, for this relatively large Ra the numerical temperature z profiles show significant deviations from those of the extended BL theory. We attribute these deviations to the plume detachments, which are not included in the extended Prandtl–Blasius BL theory. To demonstrate this we show in (*b*) time averaged temperature z profiles at a fixed x value, namely along the middle line $x = L/2$, i.e. $\Theta(\xi)|_{x=L/2} = (T|_{x=L/2} - T_t)/\Delta$. Here the plume activity is expected to be weaker than in the regions near the sidewalls, which contribute to the area averaged profile in (*a*). Indeed DNS and BL theory agree satisfactorily along the centreline.

This good agreement is remarkable as originally the Prandtl–Blasius BL theory has been derived for semi-infinite or at least long flat plates.

For $Ra = 10^8$ there are differences between the numerical and the BL theory profiles, namely, the numerical profiles are somewhat smoother than those from the BL theory (figure 4*a*). At this relatively large Ra such differences are not unexpected, because of the enhanced plume activity at larger Ra, which is not included in the extended BL theory. The plume activity is not homogeneous in the horizontal direction and the area averages in evaluating $\Theta(\xi)$ in the upper figure is taken over the whole container width $0 \leqslant x \leqslant L$, including also the neighbourhoods of the sidewalls, where the plume convection is preferentially strong. The influence of the plume convection can be confirmed by comparing with the numerical, only time averaged z profiles along the middle line $x = L/2$ (see figure 4*b*). These profiles show good agreement

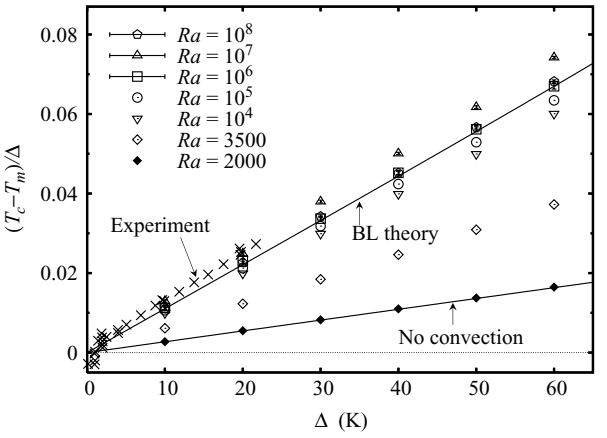

FIGURE 5. Relative deviation $(T_c - T_m)/\Delta$ of the horizontally area (and time) averaged centre temperature T_c from the arithmetic mean temperature T_m in terms of Δ versus the temperature difference Δ for water at fixed $T_m = 40\,^\circ$C for various values of Ra. The nearly linear increase means that $T_c - T_m = \text{const}\Delta^2 + h.o.t.$ The symbols $\times$ correspond to the experimental data in Ahlers *et al.* (2006) for the apparatus of 50.62 cm height. The symbols including the horizontal lines indicated in the upper left corner show the data including the error bars. The error bars given for the numerical data for $Ra = 10^6$, 10^7, and 10^8 are smaller than the sizes of the symbols.

with the extended BL theory, much better than those in the upper panel. We attribute this to the expectation that the plume detachment near $x = L/2$ is less than that near the sidewalls, and thus the BL approximation should be more reasonable along the middle line. It could be objected that the observed deviations might be due to the influence of the sidewalls, which are included in the horizontal surface averages but excluded for the centreline, with only time averaging. To clarify this point we have performed a DNS with lateral periodic boundary conditions and $\Gamma = 2$. The numerically obtained profiles (not shown here) are very close to the surface and time averaged profiles of figure 4(a) rather than to the time averaged centreline profiles in figure 4(b). This supports the conclusion that it is the plume flow and temporal dynamics of the BLs, which is the main reason for the observed discrepancy between the Prandtl–Blasius BL theory and the area averaged DNS profiles.

Nevertheless, in spite of the large deviations in the z-(or ξ-)dependence of the area averaged temperature profiles as shown in figure 4(a), the centre temperature T_c obtained from the extended BL theory (Ahlers *et al.* 2006) still very nicely agrees with that calculated with DNS. This is confirmed in figure 5, showing T_c as a function of the NOBness Δ for various Ra, ranging from 2×10^3 to 10^8. In figure 6 we display the T_c shift for fixed $\Delta = 40\,$K and $T_m = 40\,^\circ$C as a function of Ra. Interestingly enough, beyond some 10^5 for Ra, the centre temperature T_c is rather independent of Ra. Only in the immediate range beyond the onset of convection, $T_c - T_m$ is pronouncedly smaller, reflecting the smooth transition to the small value of $T_c - T_m$ in the non-convecting state. The Ra dependence of T_c is not monotonous, what we attribute to transitions between the various coherent RB flow patterns in the considered Ra range.

The results shown in figure 6 are consistent with previous findings (Lohse & Grossmann 1993) that in the Ra range from onset of convection up to about $Ra \approx 5 \cdot 10^7$ the flow only successively looses its spatial coherence. In this Ra range

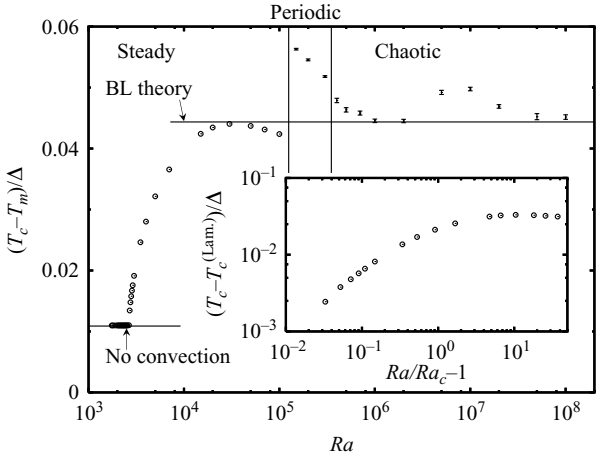

FIGURE 6. $(T_c - T_m)/\Delta$ versus Ra for water at fixed $T_m = 40\,^\circ\mathrm{C}$ and $\Delta = 40\,\mathrm{K}$. Inset: deviation of T_c from the centre temperature in the laminar case $T_c^{(lam)}$ at the onset $Ra_c = 2590$ of thermal convection at $\Gamma = 1$. Note the strong variation of T_c in a range slightly above $Ra = 10^5$, which we attribute to transitions between different coherent flow structures.

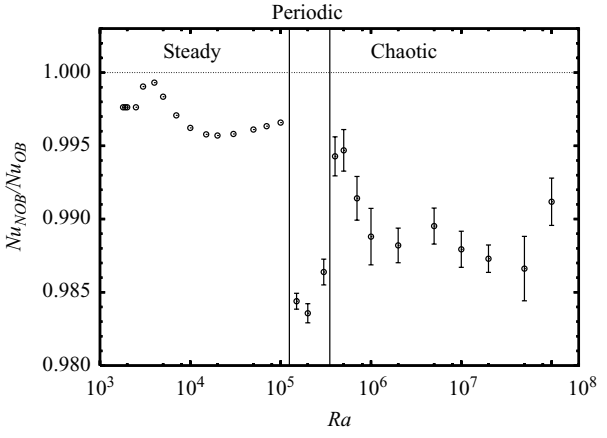

FIGURE 7. Nusselt number ratio Nu_{NOB}/Nu_{OB} versus Rayleigh number Ra for water at fixed values for $T_m = 40\,^\circ\mathrm{C}$ and $\Delta = 40\,\mathrm{K}$. It is also indicated where we are in the steady, periodic or chaotic regime.

the relative coherence length $\ell_{coherence}/L$ decreases from values far above 1 to values of order $1/6$, see figure 1 of Sugiyama *et al.* (2007) in which we have calculated $\ell_{coherence}/L$ as a function of Ra, based on the unifying theory of Grossmann & Lohse (2000, 2001, 2002, 2004). Only for Ra beyond this transition range up to some 10^7, in which spatially coherent structures are gradually lost, the heat convection is fully turbulent and the pdf of the fluctuations becomes exponential instead of being Gaussian.

4. Mean heat flux

Similarly to T_c, the Nusselt number ratio Nu_{NOB}/Nu_{OB} displays an only weak dependence on Ra (see figure 7). This ratio has been written in (1.2) in terms of two factors, F_Δ and F_λ. The latter one measures the changes of the thermal BL widths caused by NOB conditions. These widths of the temperature profile are sketched in

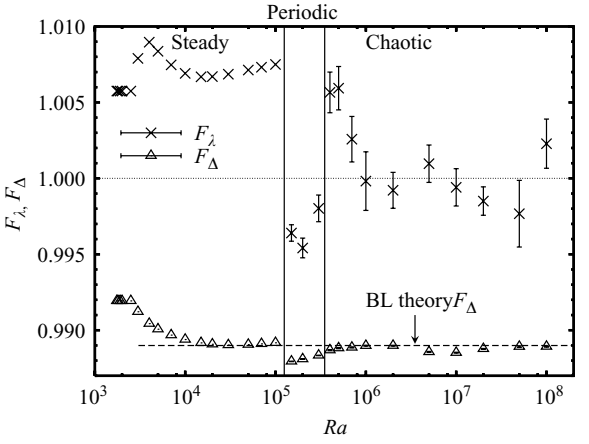

FIGURE 8. F_λ and F_Δ (defined in (1.2) and in the text before) versus Rayleigh number Ra for water at fixed values for $T_m = 40\,^\circ$C and NOBness $\Delta = 40$ K. The dashed line corresponds to F_Δ resulting from the BL theory developed in Ahlers *et al.* (2006). Reasonable agreement between BL theory and DNS is observed. F_λ in the presently considered water case is compatible with $F_\lambda = 1$ for larger Ra, as in experiment. The significant Ra-dependence for smaller and medium Ra seems to reflect the changes of the coherent flow structures still present at these Ra. In particular, one recovers the window of quite different behaviour slightly above $Ra = 10^5$.

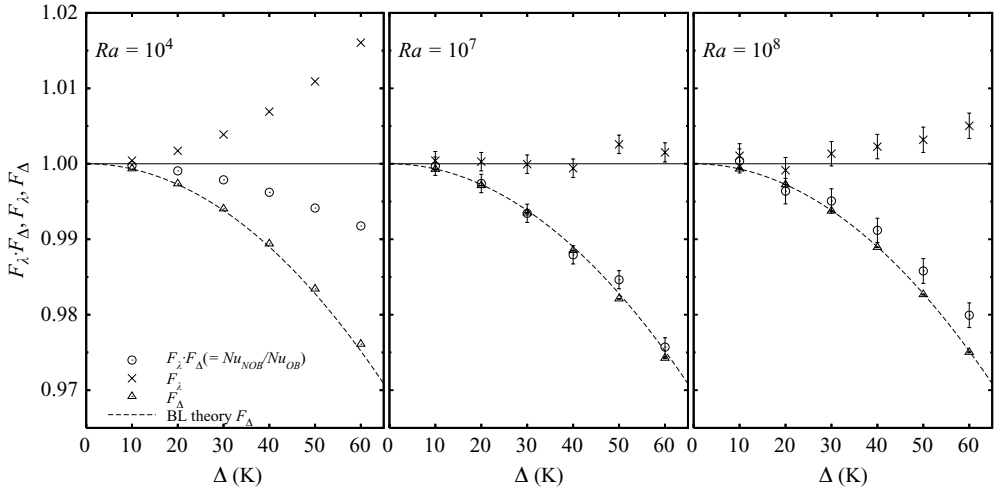

FIGURE 9. Nusselt number ratio $Nu_{NOB}/Nu_{OB} = F_\lambda \cdot F_\Delta$ together with the factors F_λ and F_Δ versus NOBness Δ for fixed Rayleigh numbers (*a*) $Ra = 10^4$, (*b*) $Ra = 10^7$ and (*c*) $Ra = 10^8$. The working liquid is water at $T_m = 40\,^\circ$C. The dashed lines correspond to F_Δ resulting from the BL theory developed in Ahlers *et al.* (2006).

figure 1; quantitatively we define them in terms of the temperature slopes at the plates.

$$\lambda_t^{sl} \equiv \frac{\Delta_t}{|\,\partial_z \langle T \rangle_{A_t,\tau}\,|}, \quad \lambda_b^{sl} \equiv \frac{\Delta_b}{|\,\partial_z \langle T \rangle_{A_b,\tau}\,|}. \tag{4.1}$$

In figures 8 and 9 we reveal the origin of the Nusselt number modification in the NOB case. In general it is a combination of the Δ-dependence of both factors F_λ and F_Δ in the product (1.2). As shown in figure 8 for fixed non-Oberbeck–Boussinesqness Δ, F_Δ displays a weak dependence on Ra for $Ra \geqslant 10^4$. This can be understood from the

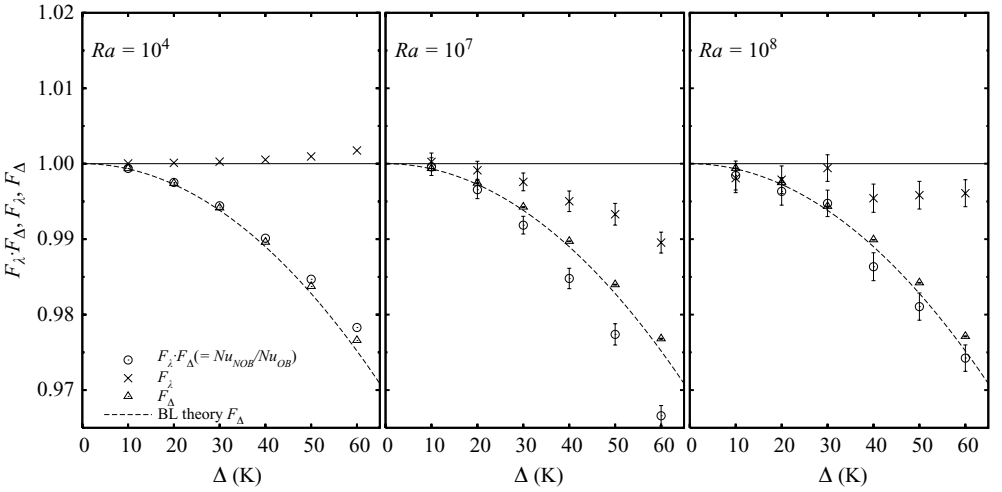

FIGURE 10. Same as figure 9, but now with a temperature independent (artificial) thermal expansion coefficient β_m, i.e. with only linear temperature dependence of $\rho(T)$ as in (1.1). The Δ-dependences of the factors F_Δ and F_λ and thus $F_\Delta \cdot F_\lambda$ are different from those in the case of fully temperature dependent $\beta(T)$.

weak Ra-dependence of the centre temperature T_c on the NOB changes of the material parameters (see figures 5 and 6), and because $F_\Delta = ((\kappa_t - \kappa_b)T_c - \kappa_t T_t + \kappa_b T_b)/(\kappa_m \Delta)$ depends on T_c only (for given T_t and T_b).

On the other hand, the factor F_λ, describing the variation of the thermal BL thicknesses, shows a rather weak but obvious dependence on the RB flow regimes. For the fully chaotic regime ($Ra \geqslant 10^6$), the deviation of F_λ from $F_\lambda = 1$ is much smaller than that of F_Δ, which indicates that Nu_{NOB}/Nu_{OB} is dominated here by F_Δ and thus by the behaviour of the centre temperature. As shown in figure 9, which displays the dependences on the NOBness Δ for the largest analysed $Ra = 10^7$ and 10^8, the Δ-dependence of F_λ happens to be very small, and for those Rayleigh numbers $F_\lambda \approx 1$ happens to be a good approximation. This might be due to an incidental combination of the temperature dependences of the material parameters $\eta(T)$, $\Lambda(T)$ and $\rho(T)$ around the chosen mean temperature $T_m = 40\,^\circ\mathrm{C}$ in the case of water. The experimental finding, reported in Ahlers *et al.* (2006), that $F_\lambda \approx 1$ in a similar Ra range, for the same $T_m = 40\,^\circ\mathrm{C}$, and for Δ up to 40 K therefore can be considered as incidental. It is not a general property of NOB Rayleigh–Bénard convection. We have also checked the influence of buoyancy on the BL widths as described by F_λ. If we disregard the T-dependence of $\beta(T)$, i. e. the nonlinear temperature dependence of $\rho(T)$ in our numerical simulations and thus have a constant $\beta = \beta_m$, F_λ shows a larger deviation from 1 at $Ra = 10^7$ and happens to be closer to 1 at $Ra = 10^4$, see figure 10, just opposite to the case with full T-dependence of $\beta(T)$. Still the nonlinear temperature dependence of ρ, i.e. the temperature dependence of β, has a relatively weak effect on F_λ and F_Δ and therefore on the Nusselt number modification.

The second conclusion we can draw from figures 8, 9 and 10 is that in all cases F_Δ is correctly described by the BL theory given in Ahlers *et al.* (2006). As F_Δ can be calculated from T_c only, this is of course to be expected, since T_c is well described by the extended Prandtl–Blasius BL theory (see figure 2).

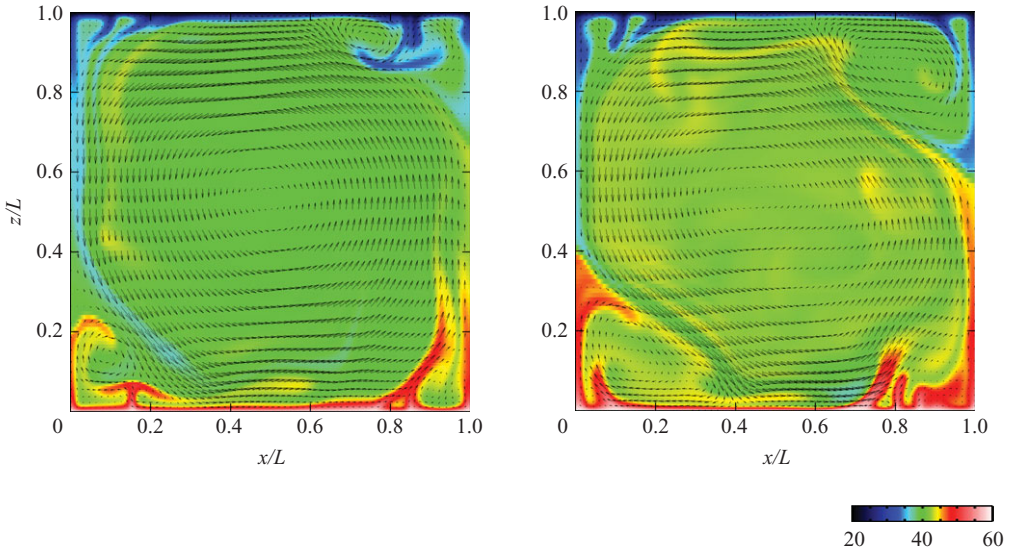

FIGURE 11. (colour) Snapshots of the velocity (arrows) and temperature (colour) fields for $Ra = 10^8$ at $T_m = 40\,^{\circ}\mathrm{C}$, working fluid water. (*a*) corresponds to the OB case (all material properties are kept temperature independent, taken at T_m), (*b*) corresponds to the NOB case, both with the same $\Delta = 40\,\mathrm{K}$. The temperature colour scheme is in °C, same in both panels.

5. The flow structure and various wind amplitudes

We focus now on the structure of the flow field or 'wind' in thermal convection. Although in our two-dimensional simulations we miss interesting but typically three-dimensional flow modes (cf. Ahlers *et al.* 2009, for a summary), even in two dimensions the velocity field is rather complex, as the snapshots in figure 11 display. Nevertheless such convection fields have mostly been described by only one single amplitude U. This wind amplitude U is a crucial parameter both in the general OB theory (Grossmann & Lohse 2000, 2001, 2002, 2004) as well as in the extended BL theory dealing with NOB effects (Ahlers *et al.* 2006). The Grossman–Lohse (GL) theory hypothesizes that one needs only one single mean wind amplitude to describe the heat transport (also for large Ra) and that this amplitude is essentially uniform throughout the cell.

The extended BL theory, developed in Ahlers *et al.* (2006) for NOB situations, assumes that such a *uniform* wind is still present even under NOB conditions and that in particular the top and bottom BLs see the very same wind amplitude $U_t = U_b = U_{NOB}$, in spite of the NOBness. The amplitude U_{NOB} is allowed to be different from U_{OB}, but for the Nusselt number calculations (not for T_c, as detailed above) its value has to be taken as a parameter of the theory. It is this character of U_{NOB} as a boundary condition for the Prandtl–Blasius BL equations which leaves the BL theory incomplete for calculating the heat transport across the RB cell. Thus neither the Reynolds nor the Nusselt number deviations under NOB conditions can be predicted, unless further input (data or assumptions) is introduced (as for instance $F_\lambda = 1$).

We organize our analysis of the two-dimensional flow structure as follows. Starting with the visualization of the dynamical flow fields, we next introduce a time averaged convective Eulerian field. Then we discuss several sensible possibilities to adequately define relevant wind amplitudes quantitatively. Finally, we present our results about

the dependences of the U amplitudes or $Re = U/(\nu L^{-1})$ numbers on the Rayleigh number Ra and the NOBness Δ.

5.1. *Dynamical features*

For RB convection in water in an aspect ratio $\Gamma = 1$ container it is known from experiment and also noticeable in our two-dimensional DNS flow as shown in the snapshots in figure 11, that a large-scale circulation (LSC) with an extension comparable to the box size L is present both in the OB and NOB cases at $Ra = 10^8$. In addition and on top of this LSC there are of course fluctuations of the $\boldsymbol{u}, T$ fields.

The time development of the numerical $\boldsymbol{u}$ field shows *reversals* in the circulation sign, in agreement with experimental observations (Sreenivasan, Bershadski & Niemela 2002; Brown, Funfschilling & Ahlers 2005; Brown & Ahlers 2006, 2007; Ahlers *et al.* 2009) and earlier numerical simulations (Hansen, Yuen & Kroening 1992). In three-dimensional experiment these reversals can occur either by rotation of the convection roll's plane or by cessation and restart; in the two-dimensional numerics of course only the latter type of reversal occurs. Several models have been developed for these reversals, see e.g. Sreenivasan *et al.* (2002); Fontenele Araujo, Grossmann & Lohse (2005); Benzi (2005); Brown & Ahlers (2007). We shall report on details of our results about the statistical properties of the reversals in our two-dimensional simulations elsewhere. In the context of the present paper these reversals only complicate the statistical analysis of the flow field, as long-time averages of the velocity field become zero and wash out the flow structures.

How then to obtain the main features of the dynamical, complex time-dependent $\boldsymbol{u}$ field? To achieve them we consider conditionally time averaged Eulerian fields as well as several profiles, which partly take the fluctuations into account too. In addition a global, energy based wind amplitude is introduced.

5.2. *Conditionally time averaged velocity fields*

To overcome the problem that long time averages due to the statistical flow reversals give zero velocity everywhere, we perform *conditioned* time averages, which take the time dependent rotational direction of the wind into account. This instantaneous rotational direction is identified by the sign of the vorticity at the centre of the box. Whenever the wind reverts its direction, before performing the standard time averaging the velocity field is mirrored along the vertical centreline. Respecting this, from the full velocity field $\boldsymbol{u}(\boldsymbol{x}, t)$ we can compute another, time averaged, complete two-dimensional Eulerian-type velocity field $\overline{\boldsymbol{u}}(\boldsymbol{x})$, in which the respective local direction of the velocity is coupled to the sign of the central vortex. Componentwise we define this conditionally time averaged flow field as

$$\begin{aligned} \overline{u_x}(x, z) &= -\mathscr{T}^{-1} \int_{t_0}^{t_0+\mathscr{T}} \mathrm{d}t\, u_x(\tilde{x}, z, t)\ \mathrm{sign}\ \omega_c(t), \\ \overline{u_z}(x, z) &= \mathscr{T}^{-1} \int_{t_0}^{t_0+\mathscr{T}} \mathrm{d}t\, u_z(\tilde{x}, z, t). \end{aligned} \tag{5.1}$$

Here $\mathscr{T}$ denotes the averaging time, sign $\omega_c(t)$ is the sign of the vorticity $\omega(x, z) \equiv \partial_z u_x - \partial_x u_z$ at the centre of the box $(x, z) = (\frac{L}{2}, \frac{L}{2})$ and $\tilde{x}$ is

$$\tilde{x} = L/2 + (L/2 - x) \cdot \mathrm{sign}\ \omega_c(t).$$

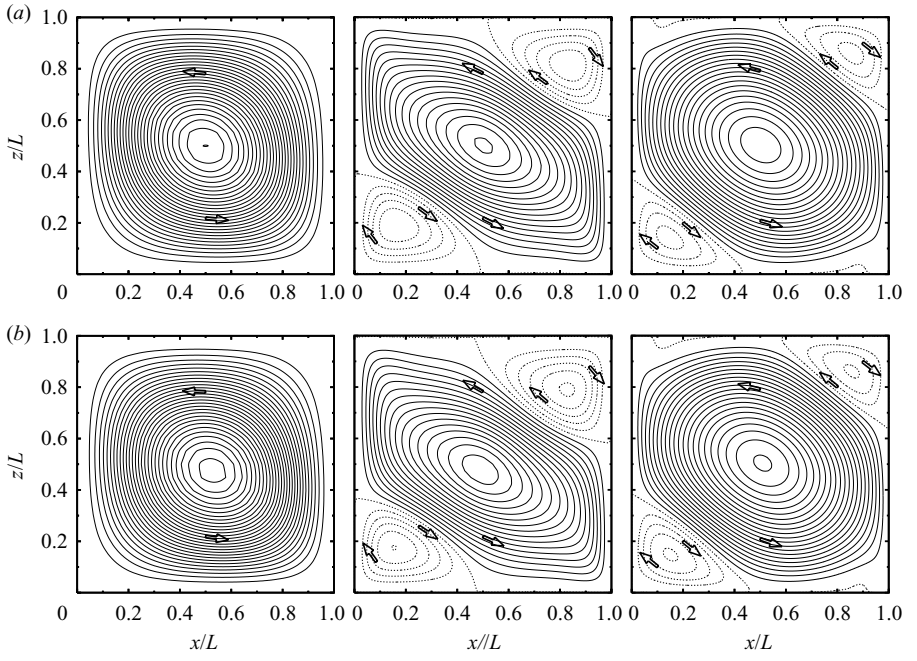

FIGURE 12. Lines of constant values for the conditionally time averaged velocity field $\overline{\boldsymbol{u}}(x, z)$ at different Rayleigh numbers $Ra = 10^4, 10^6, 10^8$ in OB convection (a) and NOB convection (b), both with the same $\Delta = 40\,\mathrm{K}$. Counterclockwise velocity direction is drawn with solid lines, while the clockwise ones are indicated by dotted lines. The OB flow structure, which already develops secondary (counter) rolls in two opposite corners, enjoys top–bottom symmetry. The asymmetry in the NOB cases is best seen in the two different amplitudes of the corner-flow rolls, identified by counting the number of their equally spaced streamlines.

In a similar manner we also define the conditionally averaged velocity squares as

$$\begin{aligned} \overline{u_x^2}(x, z) &= \mathscr{T}^{-1} \int_{t_0}^{t_0+\mathscr{T}} \mathrm{d}t\, u_x^2(\tilde{x}, z, t), \\ \overline{u_z^2}(x, z) &= \mathscr{T}^{-1} \int_{t_0}^{t_0+\mathscr{T}} \mathrm{d}t\, u_z^2(\tilde{x}, z, t). \end{aligned} \tag{5.2}$$

Rather than conditioning on the sign of the vorticity at the centre, one could also condition on the sign of the total angular momentum, as has been done by van Heijst, Clercx & Molenaar (2006) (which minimizes the contributions of some high-frequency oscillations), but for the purpose of this paper the difference between these two types of conditional averaging has turned out not to be relevant.

Conditionally time averaged fields $\overline{\boldsymbol{u}}(\boldsymbol{x})$, being time independent objects, allow to visualize the persistent spatial structures in the flow field. Some conditionally time averaged fields obtained for different Ra numbers are shown in figure 12.

Note again the large circulation roll in the centre range but also the secondary counter-rotating rolls in two opposite corners. We remark that such secondary circulation rolls in nearly-two-dimensional convection have been experimentally detected by Xia, Sun & Zhou (2003). In our simulations secondary rolls appear for $Ra > 10^5$. We interpret the secondary rolls as caused by boundary layer separations, which are known to occur when a flow is heading a perpendicular wall. They might be

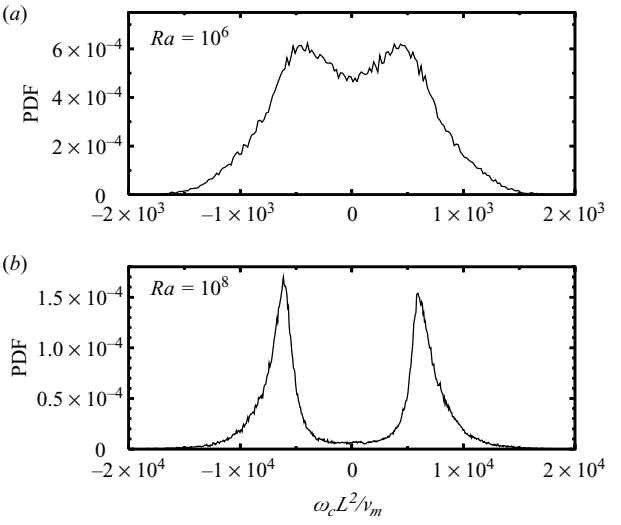

FIGURE 13. Probability density function of the vorticity ω_c at the cell centre at $Ra = 10^6, 10^8$.

considered as kind of 'wakes' behind the separation. Remarkably, the secondary roles are of considerable size for the BL separations of the up and down going flows, which approach the top and bottom plates, respectively, but are nearly invisible for the horizontal ones, which approach the sidewalls (at least for these Rayleigh numbers). This might be attributed to the plume creations in the BLs on the bottom and top plates, which affect the horizontal but not the vertical sections of the flow.

We emphasize that the convergence of the statistics implies that a centre-point symmetry should be established for the conditionally time averaged field $\overline{\boldsymbol{u}}$. Indeed, within 5 % precison we achieve such a centre-point symmetry in our numerical simulations. As we shall see later this accuracy is by far sufficient to discriminate the main NOB effects in comparison to the OB results.

For information we add the probability density function (PDF) of the centre vorticity ω_c, (non-dimensionalized by the molecular vorticity $\nu_m L^{-2}$), see figure 13. Already for $Ra = 10^6$ two preferred values of the LSC can be recognized, reflecting clockwise and counter-clockwise rotation of the large scale convection roll. For $Ra = 10^8$ the two preferred vorticities are even more pronounced, reflected by the sharp peaks in the PDF. While in the chaotic phase ($Ra \approx 10^6$) the PDF is still broad, the flow cessations at $Ra \approx 10^8$ are very fast events, since the small probability for $\omega_c = 0$ suggests that the flow changes its direction more or less momentarily, leaving only a very small probability to find $\omega_c = 0$.

5.3. *Wind profiles: amplitudes*

Because even the conditionally time averaged velocity field as shown in figure 12 has a rich spatial structure, it is not immediately apparent how to define 'a characteristic single wind velocity amplitude U' unambiguously. Several definitions have been proposed in the literature. In the present section we introduce various possible definitions for wind amplitudes U and corresponding Reynolds numbers $Re = UL/\nu_m$, by investigating global measures as well as local ones, and also certain profiles.

(i) Global. A global measure for the strength (amplitude) of the convection can be based on the volume average. While the velocity average over the full volume is of course zero, we can consider the velocity r.m.s. average and obtain the energy-based

wind amplitude

$$U^E \equiv \sqrt{\left\langle \frac{1}{2}\left(u_x^2 + u_z^2\right)\right\rangle_{V,t}} = \sqrt{\left\langle \frac{1}{2}\left(\overline{u_x^2} + \overline{u_z^2}\right)\right\rangle_{V}}. \tag{5.3}$$

Apparently, both the primary centre roll as well as the secondary rolls contribute to the value of U^E. While the primary roll covers the whole interior, which is expected to be mixed by turbulence and therefore has essentially uniform temperature T_c, the secondary rolls experience either the cooler top or the hotter bottom regions only. Since under NOB conditions the viscosity deviations are different near the top and bottom (and, of course, from the bulk), the secondary rolls are expected to have different properties among each other as well as relative to the primary centre roll. U^E represents a well-defined mixture of all of them.

(ii) Local. To deal with the top and bottom differences, local wind amplitudes may be introduced by considering the values of the conditionally time averaged field $\overline{\boldsymbol{u}}(\boldsymbol{x})$ at particular spatial positions $\boldsymbol{x}_j$ in the flow field. Particular positions are e.g. those, where the conditionally time averaged velocity field $\overline{\boldsymbol{u}}$ has peak values U^{P_j} along some vertical lines, labelled by j. In the following, we shall consider such local peak amplitudes U^{P_j} at peak positions on vertical lines with abscissas $x_j = \frac{3L}{4}$, $\frac{L}{2}$ and $\frac{L}{8}$. These points P_j roughly correspond to the positions where the main primary circulation roll is strongest ($x_1 = \frac{3L}{4}$), to the flow maxima along the centreline of the container ($x_2 = \frac{L}{2}$) and to the region where the counter-rotating roll is well developed ($x_3 = \frac{L}{8}$).

(iii) Profiles. Mixed type wind amplitudes, neither fully global nor fully local, can be introduced as area averages or rather, in two dimensions, as line averages. The areas (lines) can either be chosen as top/bottom plate parallel or as sidewall parallel. The corresponding area averaged wind amplitudes then either, as in the case of plate parallel averaging, depend on the height z of the area (line) and lead to z-dependent wind profiles; this is relevant for the horizontal wind and its vertical profile $U_x(z)$. Or they depend, as in the case of vertical line averaging, on the x-distance to the sidewalls and lead to x-dependent profiles; these are relevant for the up rising or down falling flow and its horizontal profile, denoted as $U_z(x)$.

Such area (line) and time averages are the relevant quantities in the well-known relations between the energy respective dissipation rates ε_u, ε_θ and the non-dimensionalized heat current density, i.e. the Nusselt number Nu. While the dissipation rates are volume averages, the Nusselt number is defined in terms of a horizontal area average, which by conservation of energy even is independent of height z. One contribution to Nu comes from the $\langle Tu_z\rangle_{A,t}$-correlation, the other one from the gradient of the temperature profile $\langle T\rangle_{A,t}(z)$. This justifies to introduce the mentioned area (line) averages also for velocity components. In particular, the vertical profile of the horizontal velocity $U_x(z)$ is of interest, as well as the horizontal profile of the vertical velocity, $U_z(x)$, precisely defined as

$$U_x(z) = \langle \overline{u_x}\rangle_{x(z)}(z), \qquad \text{and} \qquad U_z(x) = \langle \overline{u_z}\rangle_{z(x)}(x). \tag{5.4}$$

where $\langle \ldots\rangle_{x(z)}$ and $\langle \ldots\rangle_{z(x)}$ represent the line averaging along the x direction for fixed z or along the z direction for fixed x.

Area averaged profiles are displayed in figure 14. Surprisingly there are small ranges with negative (positive) $U_x(z)$ of the area averaged horizontal velocity in the immediate vicinity of the bottom (top) plates. Formally, their origin is that the area averaged profiles as $U_x(z)$ take notice of the sign of the corresponding local velocities

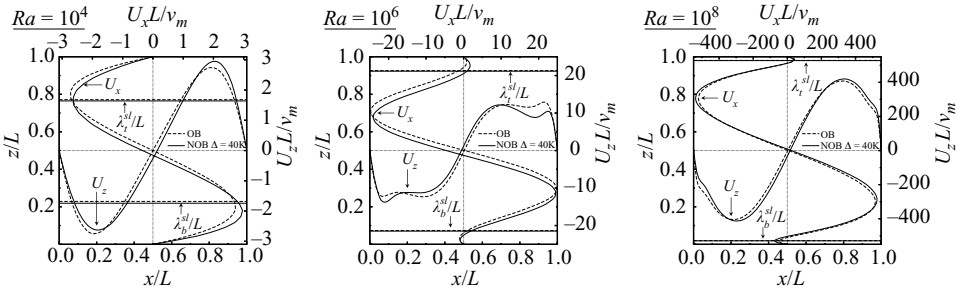

FIGURE 14. The vertical and horizontal velocity profiles $U_x(z)$ and $U_z(x)$ as derived from the conditionally time averaged velocity components $\overline{u_x}$ and $\overline{u_z}$ at three different Ra numbers 10^4, 10^6, 10^8. The abscissa and ordinate scales are the dimensionless width and height. The upper scales show the horizontal velocity profiles non-dimensionalized with v_m/L, i.e. $Re_x(z)$; the right scales show the vertical velocity's $U_z(x)$ profiles, also non-dimensionalized by v_m/L. Note the increase of the $Re_{x,z}$ scales with increasing Ra. Dashed lines indicate the OB case, full lines the NOB case. In both cases $\Delta = 40\,\mathrm{K}$. Also indicated are the corresponding thermal slope BL widths $\lambda^{sl}_{b,t}$, which strongly decrease with Ra.

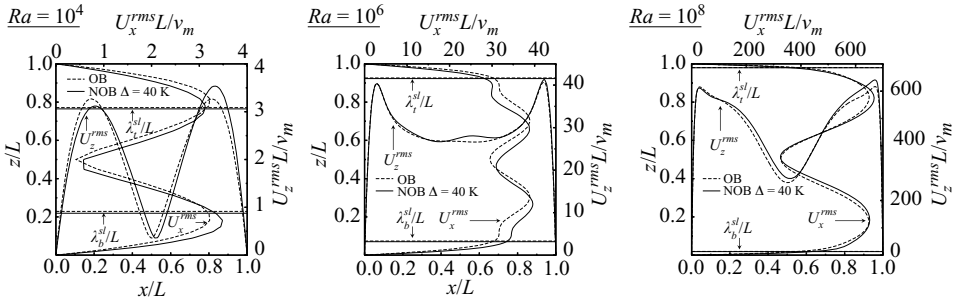

FIGURE 15. The vertical and horizontal rms velocity profiles $U_x^{rms}(z)$ and $U_z^{rms}(x)$ as derived from the area averaged r.m.s. fields $\sqrt{\langle u_x^2\rangle_{x,t}}(z)$ and $\sqrt{\langle u_z^2\rangle_{z,t}}(x)$ at three different Ra numbers 10^4, 10^6, 10^8. The scaling schemes for the abscissa and ordinate, the representations of the lines and the conditions are the same as in figure 14. Note the different magnitudes (scales) for the different Ra.

and these in the secondary rolls are opposite to that of the centre roll. Thus one clearly sees the effects of the secondary rolls in the inversion of the vertical profile in the neighbourhood of the bottom and top plates. Physically this might be interpreted that plumes in this range of small distances from the plates are mostly advected in the opposite direction until they come farther away. One also observes broken top–down symmetry. This is caused by the secondary rolls, since these cover regions of different temperatures.

(iv) r.m.s. profiles. In addition to area averages of the (conditionally time averaged) velocity components themselves one might also wish to analyse area averages of the r.m.s. fields of the corresponding components, defined as

$$U_x^{rms}(z) = \sqrt{\langle \overline{u_x^2}\rangle_{x(z)}}\,(z) = \sqrt{\langle u_x^2\rangle_{x(z),t}}\,(z), \quad \text{and} \quad U_z^{rms}(x) = \sqrt{\langle \overline{u_z^2}\rangle_{z(x)}}\,(x). \tag{5.5}$$

These are displayed in figure 15.

In the r.m.s. profiles $U^{rms}_{x,z}$ one also observes the kink and the broken symmetry as in the averaged velocity profiles $U_{x,z}$ in figure 14, but no change in sign, of course. The preferentially strong plume convection near the sidewalls is clearly reflected in

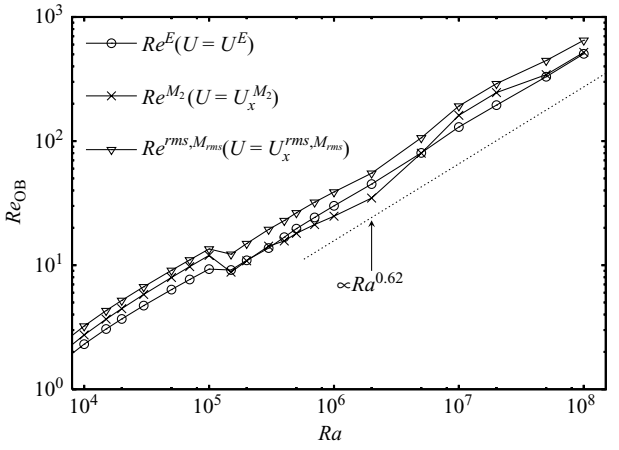

FIGURE 16. Several energy and peak based Reynolds numbers in the OB case versus Ra for water at $T_m = 40\,^{\circ}\mathrm{C}$. The temperature difference between bottom and top is $\Delta = 40\,\mathrm{K}$.

the $U_z^{rms}(x)$ profiles and their sharper peaks as well as apparently significantly smaller boundary layers than in the $U_x^{rms}(z)$ profiles. In the vertical profiles of $U_x^{rms}(z)$ the near-wall inversion (owing to the opposite sign of the velocity in the secondary and centre rolls) is not present, in contrast to the amplitude averaged $U_x(z)$ profile in figure 14, since U_x^{rms} is positive everywhere. Instead, one recognizes the signature of the secondary roll effect as the steep slope in the U_x^{rms} profile between the plate and its maximum position.

Experimentally, often Lagrangian flow properties as, for example, the plume turnover times are used to characterize in particular the large-scale coherent flow. We emphasize that such features should be identified in the $U_x(z), U_z(x)$ profiles. The $U_x^{rms}(z), U_z^{rms}(x)$ profiles, instead, reflect the energy strengths of the considered components. In the following we will use two different velocity amplitudes defined on the local maxima of the horizontal profiles $U_x(z)$ and $U_x^{rms}(z)$, denoted respectively as $U_x^{M_2}$, $U_x^{rms,M_{rms}}$, where the super-script M_2 indicates the second (and positive) maximum on $U_x(z)$. In figures 14 and 15, the z distances, at which the velocities have the values $U_x^{M_2}$ and $U_x^{rms,M_{rms}}$, respectively, are comparable. Both are located within the thermal BL at $Ra = 10^4$ while they are outside at $Ra = 10^6$ and 10^8. Furthermore, NOB effects on the maximum positions are observed to be Rayleigh number independent, in the sense that one observes shifts of comparable size towards the bottom plate at $Ra = 10^4$ and 10^6. However, as we shall see later, one notices slight differences because the non-trivial spatio-temporal flow structure is differently reflected in the U_x and U_x^{rms} profiles.

5.4. *Scaling of amplitudes with Ra, Oberbeck–Boussinesq case*

Having described the flow structures and the definitions of several relevant measures for the magnitude of the thermally driven convection, we now offer our results on the Ra- and Δ-dependence of the various U amplitudes and the corresponding Reynolds numbers $Re = U/(\nu_m L^{-1})$. We start with the OB case, i.e. having temperature independent material parameters throughout the container, their values taken at the given arithmetic mean temperature T_m. Figure 16 shows the scaling of Re^E, Re^{M_2} and $Re^{rms,M_{rms}}$ with Ra for the OB case.

The structure in the Re_{OB}^E versus Ra curve around $Ra \approx 10^5$ is due to changes in the still present coherent flow patterns, implied by the boundary conditions. They

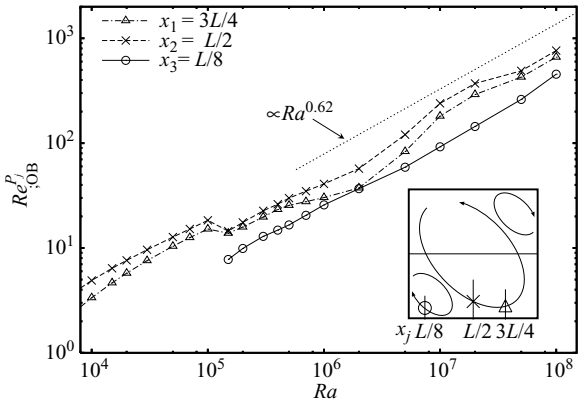

FIGURE 17. Reynolds numbers Re^{P_j} at $x_j = \frac{3L}{4}$(triangles), $\frac{L}{2}$(crosses), $\frac{L}{8}$ (circles) in the OB case versus Ra for water at $T_m = 40\,^\circ\mathrm{C}$; again $\Delta = 40\,\mathrm{K}$. The inset shows a sketch of the flow with the positions of the velocity peaks being indicated by the three different symbols.

are observed in the Nu behaviour too (not shown here), and are also detected in experiment, see for instance Threlfall (1975). For water as the working fluid the typical spatial coherence length (in terms of L) of the coherent flow structures has decreased to about order 0.1 only in the Ra range between some 10^7 and 10^8 (Sugiyama *et al.* 2007). A power-law fit, $Re^E = cRa^\gamma$, in the range $7 \cdot 10^5 \leqslant Ra \leqslant 10^8$, corresponding to the transition range from chaotic to turbulent behaviour, gives the exponent $\gamma = 0.62$.

The behaviour of the Re^{P_j} at $x_j = \frac{L}{8}, \frac{L}{2}, \frac{3L}{4}$, see figure 17, is more noisy but scaling-wise similar to (at least compatible with) Re^E, although in Re^{P_j} the spatial structures of the flow field are well taken into account. Re^E is more robust with respect to the convergence of the statistics. Experimentally at moderate Ra the Reynolds numbers may scale differently, cf. Lam *et al.* (2002). In that reference the Reynolds number based on the maximum horizontal velocity near the bottom plate outside the BL is reported to scale $\propto Ra^{0.70}$ for $Ra \leqslant 2 \cdot 10^7$ and $\propto Ra^{0.495}$ for $Ra \geqslant 2 \cdot 10^7$. The set of exponents γ obtained in our simulation for Re^E and the three $Re^P_{x_j}$ ($\gamma \simeq 0.62$) are therefore reasonably consistent with experimental findings.

5.5. *Scaling of amplitudes with Ra and* Δ*, non-Oberbeck–Boussinesq case*

We now study the NOB case, starting with the conditionally time averaged velocity field $\overline{\boldsymbol{u}}$, which now is bottom–top asymmetric. In particular, there is thinning/thickening of the bottom/top kinetic BLs. For the wind amplitudes based on the peak values of $\overline{\boldsymbol{u}}$ along vertical lines we can distinguish between bottom and top peak velocities $U_b^{P_j}$ and $U_t^{P_j}$ for the various x_j-lines. As shown in figure 18, the ratio $Re_b^{P_{x=L/2}}/Re_t^{P_{x=L/2}}$ characteristic for the peak velocities taken in the main primary circulation roll converges to unity as Ra is increased up to $Ra \approx 10^8$ and Δ kept fixed. This shows that for the primary roll, which scans the bulk of the convection cell, a single velocity amplitude develops in the turbulent range also under NOB conditions, just as assumed in the BL theory introduced in Ahlers *et al.* (2006, 2007). This is also found in figure 19, where the peak velocity scales are replace by $U_x^{M_{1,2}}$ and $U_x^{rms,M_{rms}}$. In particular, the large variation in the bottom/top Reynolds number ratio in figure 18, which reflects the spatial inhomogeneity in the velocity distribution, is smoothened by

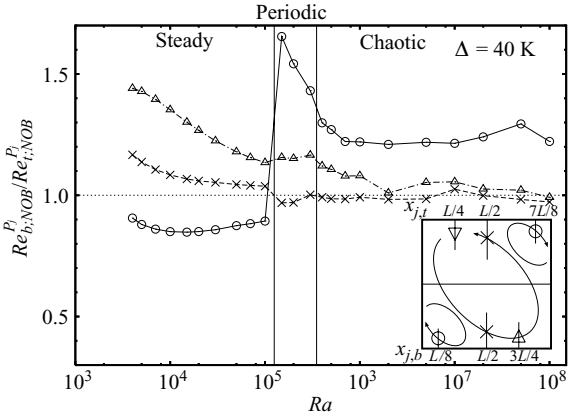

FIGURE 18. Ratio $Re^{P_j}_{b;NOB}/Re^{P_j}_{t;NOB}$ versus Ra for the different peak positions in the cell. Note that due to the centre-point symmetry of the conditionally time averaged field $\overline{\boldsymbol{u}}$, the peak positions along the lines $x_{j,b} = \frac{L}{8}, \frac{L}{2}, \frac{3L}{4}$ for the bottom part have to be compared with the peak positions along $x_{j,t} = \frac{7L}{8}, \frac{L}{2}, \frac{L}{4}$ for the top part. The figure shows that the main convection loop for large Ra establishes a uniform velocity amplitude, while the secondary counter-rotating rolls do not enjoy the same property. Instead, since they are BL-dominated rather than bulk-dominated, they show significant NOB bottom–top asymmetry. Note that the accuracy of this test may be assessed from the level of the centre-point asymmetry we had in the OB case, which was always below 5 %. Therefore we may conclude that in the chaotic regime there are no NOB deviations distinguishable for the $Re^{P_j}_{b;NOB}/Re^{P_j}_{t;NOB}$ ratios at the two positions $x_{2,3} = \frac{L}{2}, \frac{3L}{4}$. But there is a significant deviation for $L/8$, i.e. for the secondary rolls' ratios.

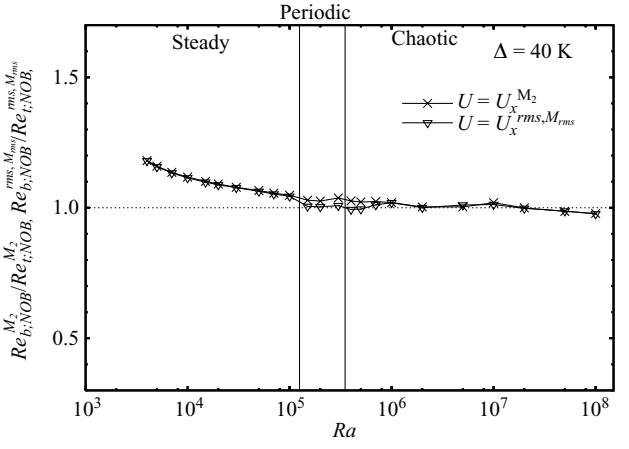

FIGURE 19. Same as figure 18, but with the peak values of the horizontal area averaged velocities $U_x^{M_2}$ and $U_x^{rms,M_{rms}}$ taken for the velocity scales.

taking the area average as indicated by the almost flat profiles of $U_x^{M_i}$ and $U_x^{rms,M_{rms}}$ in figure 19.

The secondary rolls, counter-rotating to the primary roll, have different wind amplitudes near bottom and top, as becomes apparent in the bottom–top ratio at the line $x_{1,b}/L = 0.125$ and its mirror at the top $x_{1,t}/L = 1 - 0.125$. The secondary roll at the warmer bottom plate is faster than the corresponding secondary roll near

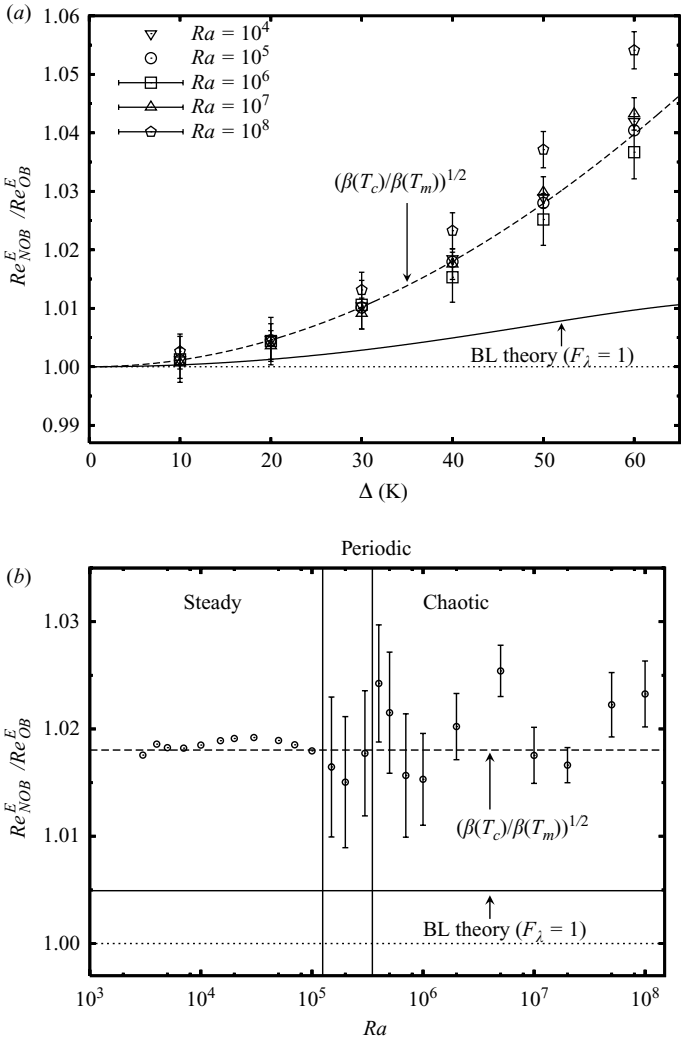

FIGURE 20. The Reynolds number ratio Re^E_{NOB}/Re^E_{OB} based on the total kinetic energy for water at $T_m = 40\,^\circ$C. (*a*) Re^E_{NOB}/Re^E_{OB} versus Δ for various choices of fixed Ra. The symbols including the horizontal lines indicated in the upper left corner show the data including the error bars. The numerical data for $Ra = 10^6$ and larger are given with statistical error bars. (*b*) Re^E_{NOB}/Re^E_{OB} versus Ra at fixed non-Oberbeck–Boussinesqness $\Delta = 40\,$K. The full line is calculated from BL theory under the assumption that $\lambda^{sl}_b + \lambda^{sl}_t = 2\lambda^{sl}_{OB}$, i.e. $F_\lambda = 1$. The dashed line indicates the limit $\Delta \to 0$ where the Reynolds number ratio approaches 1. For the explanation in terms of the T-dependence of β see text, in particular (5.6).

the top plate. We understand this from the smaller viscosity near the bottom due to the higher temperature. For the working fluid water and $\Delta = 40\,$K the bottom–top asymmetry is as large as $\approx 25\,\%$

We therefore calculated the NOB/OB ratio of Re^E versus Δ for various values of Ra as well as versus Ra at fixed non-Boussineqness $\Delta = 40\,$K. This is shown in figure 20. We observe that NOB effects are clearly present, although rather weak only, of order 2 %, indicating a small increase of the kinetic energy based mean velocity. The reason for the rather small NOB effect on the global wind amplitude in spite of the large changes of the bottom and top velocities is that the secondary rolls only

contribute a limited fraction to the global volume average. Also, the OB-to-NOB changes of the velocities of the secondary rolls are opposite in sign, one contributing a larger (bottom), the other contributing a smaller (top) amplitude. The remaining net change of the global amplitude U^E thus again is due to the nonlinear temperature dependences of the material parameters, producing different secondary roll velocities at bottom and top. This crucial importance of the nonlinearities in the temperature dependence of the material properties was already found in Ahlers *et al.* (2006).

Let us recall that the Nusselt number becomes smaller with increasing Δ as was shown in figure 9. Therefore, although the global Reynolds number ratio is enhanced under NOB conditions, the overall heat transport is attenuated. We have also included in figure 20 a comparison with BL theory. We remind that to make this theory predictive an additional assumption on F_λ (e.g. $F_\lambda \simeq 1$) has to be made. Note that the extended BL theory in this form underestimates the NOB effect on the wind.

As the origin of this discrepancy we can now identify the effect of the temperature dependence of the thermal expansion coefficient, which by (Prandtl-)Ansatz is not included in the BL equations in Ahlers *et al.* (2006). For this explanation we offer the following argument. As a naive estimate one can assume that the volume averaged velocity scale U^E in essence should coincide with the free-fall velocity, that is $U^E \simeq \sqrt{gL\beta(T)\Delta}$. This corresponds to the scaling $Re \sim Pr^{-1/2}Ra^{1/2}$. Assuming then that the temperature of the bulk is dominated by T_m and T_c respectively in the OB and NOB cases, one gets

$$\frac{Re^E_{NOB}}{Re^E_{OB}} \sim \left(\frac{\beta(T_c)}{\beta(T_m)}\right)^{1/2}. \tag{5.6}$$

This is in encouraging agreement with the DNS data, cf. figure 20. We note that also $Re^E_{NOB}/Re^E_{OB} \sim (\beta(T_c)/\beta(T_m))^\gamma$ with $\gamma = 0.62$ is consistent with the data of figure 20(*a*), rather than $\gamma = 1/2$ as suggested in (5.6). This finding implies $Re^E_{NOB} \sim (\beta_c \Delta L^3/(\kappa_m \nu_m))^\gamma$, similar to $Re^E_{OB} \sim (\beta_m \Delta L^3/(\kappa_m \nu_m))^\gamma = Ra^\gamma$ as seen for the OB case of figure 16. Note that of course $\beta_c \Delta L^3/(\kappa_m \nu_m)$ is not the control parameter Ra.

As a further support of our argument emphasizing the importance of the temperature dependence of the thermal expansion coefficient in the bulk we also calculated Re^E_{NOB}/Re^E_{OB} for a hypothetical liquid, which has all material properties as water, apart from the thermal expansion coefficient β, which we keep constant at β_m, see figure 21. Indeed, Re^E_{NOB} now only shows a smaller than 1 % deviation from Re^E_{OB}, even at $\Delta = 60\,\mathrm{K}$. These tiny deviations from $Re^E_{NOB}/Re^E_{OB} = 1$ are consistent with the results from the Prandtl–Blasius theory with the additional assumption $F_\lambda = 1$. Figure 21 thus confirms that the main origin of the NOB deviation in the Reynolds number Re^E is the temperature dependence of the thermal expansion coefficient, an effect which clearly cannot be captured in the Prandtl–Blasius BL theory.

The changes of Re^E caused by the loss of OB conditions can be analysed quantitatively in detail. For this we decompose the volume average into three regions, corresponding to the main, primary, LSC and the two secondary lower and upper corner rolls.

$$(Re^E)^2 = a_{LSC}\left(Re^E_{LSC}\right)^2 + a_{lower}\left(Re^E_{lower}\right)^2 + a_{upper}\left(Re^E_{upper}\right)^2. \tag{5.7}$$

Here a_α denotes the ratio of the area A_α occupied by the region α, with α = LSC, lower, or upper secondary roll, to the total area, and Re^E_α is the Reynolds number based on the kinetic energy averaged over each area A_α

$$Re^E_\alpha = \frac{LU^E_\alpha}{\nu_m} \quad \text{with} \quad U^E_\alpha = \sqrt{\frac{1}{A_\alpha}\int_{A_\alpha} \mathrm{d}^2\boldsymbol{x}\ \frac{1}{2}\left(\overline{u_x^2}(\boldsymbol{x}) + \overline{u_z^2}(\boldsymbol{x})\right)}. \tag{5.8}$$

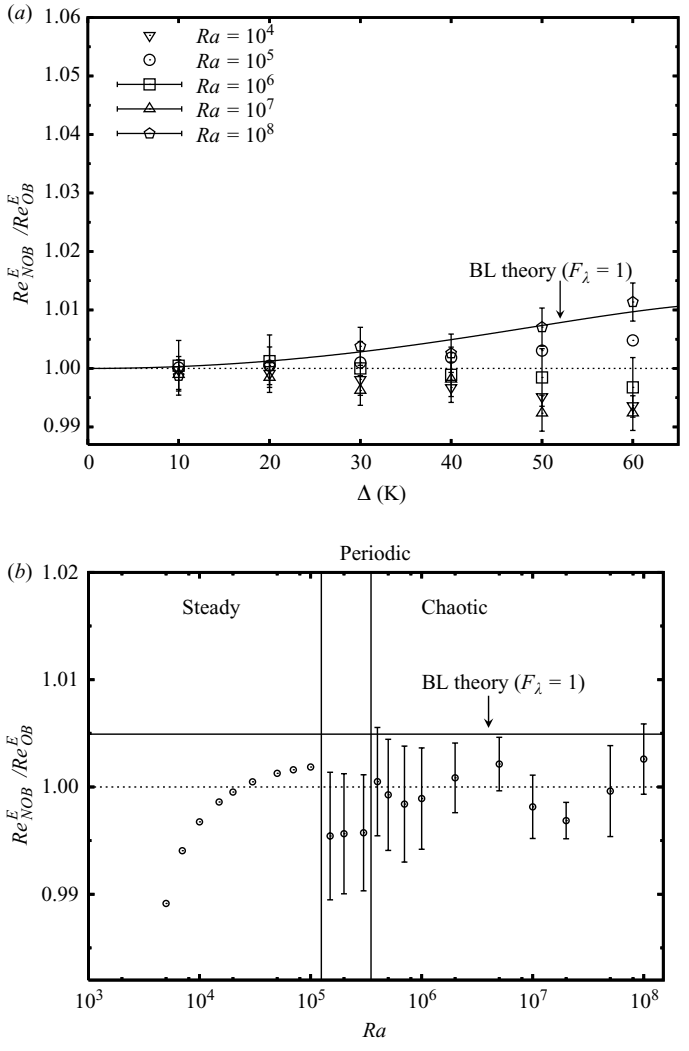

FIGURE 21. Same as figure 20(*a*), but here with only linear dependence of $\rho(T)$ on the temperature T, meaning that the thermal expansion coefficient $\beta(T)$ is set to the constant value β_m. Note that under this approximation there is good agreement with the results from BL theory and $F_\lambda = 1$ for large Ra, which means that the thermal convection takes significant notice of the full T-dependence of the thermal expansion coefficient β. BL theory misses that per construction.

The lower secondary roll is characterized by a clockwise rotation and negative values of the $\overline{\boldsymbol{u}}(\boldsymbol{x})$-stream function $\psi(x,z) = \int_0^z \mathrm{d}\hat{z}\ \overline{u_x}(x,\hat{z})$. The region A_{lower} of the lower corner roll is defined by $\psi \leqslant 0$, $x \leqslant L/2$ and $z \leqslant L/2$, while for the upper corner roll we have $\psi \leqslant 0$, $x \geqslant L/2$ and $z \geqslant L/2$. The remaining region comprises the primary main roll, LSC.

The insets of figure 22 show the (squared) NOB/OB Reynolds number ratios $(Re^E_{\alpha,NOB})^2/(Re^E_{\alpha,OB})^2$ for each region α at $Ra = 10^8$. The insets both in the upper and lower panels reveal that the largest NOB enhancement of the kinetic energy occurs inside the lower corner secondary roll (near the warmer bottom plate), as already found in the bottom–top asymmetry of the peak velocity $Re^{P_{x=L/8}}_{b,NOB}/Re^{P_{x=7L/8}}_{t,NOB}$

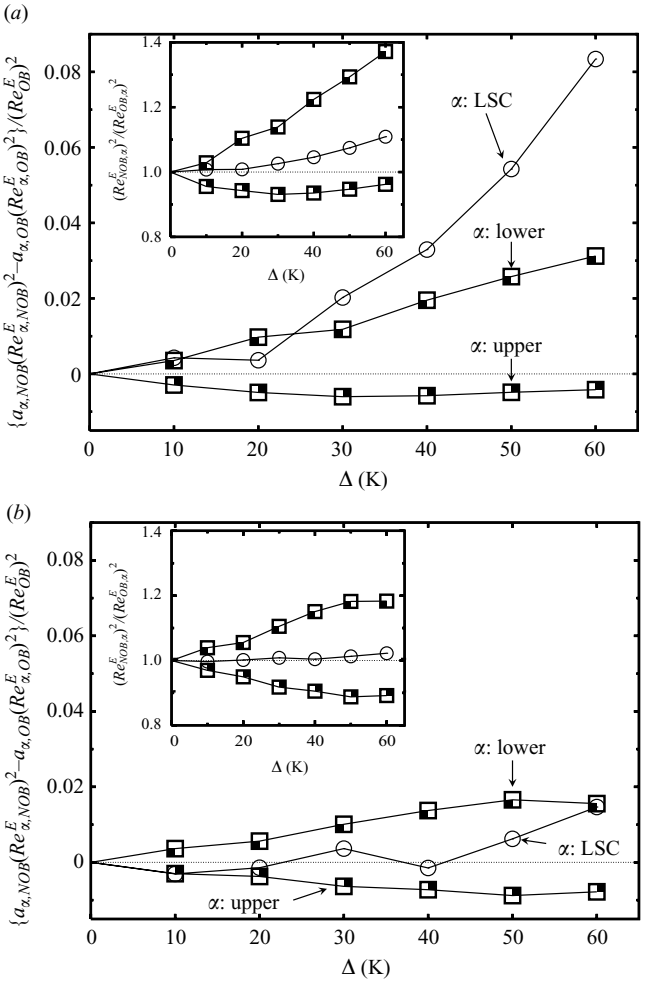

FIGURE 22. The relative deviation of the kinetic energy $\{a_{\alpha,NOB}(Re^E_{\alpha,NOB})^2 - a_{\alpha,OB}(Re^E_{\alpha,OB})^2\}/(Re^E_{OB})^2$ in region α due to NOB effects for water at $Ra = 10^8$ and $T_m = 40\,^\circ$C. The label α denotes the portion of the LSC roll in the centre region (as indicated by the solid lines in figure 12), or the secondary counter-rotating rolls in the lower and upper corners (given by the dashed lines in figure 12). The partition is determined by using the sign of $\psi = \int_0^z \mathrm{d}\hat{z}\ \overline{u_x}^c(x, \hat{z})$, e.g. the lower corner flow is defined as the region satisfying $\psi \leqslant 0$, $x \leqslant L/2$ and $z \leqslant L/2$. (*a*) the full temperature dependence is considered for the buoyancy $g(1 - \rho/\rho_m)$ as given in Table 1. (*b*) restriction to only linear dependence of the buoyancy with respect to the temperature T, i.e. the thermal expansion coefficient $\beta(T) = \beta_m$ is constant. The insets show the (squared) NOB/OB Reynolds number ratio in the each region.

in figure 18. But even this enhancement does not impact significantly on the overall Re^E change because the volume ratio of each corner flow is only $a_{lower} = a_{upper} \approx 9\,\%$, i.e. the spatial extension of both secondary rolls is about the same, while the main volume fraction is $a_{LSC} \approx 82\,\%$. This is even more pronounced in the OB case, where $a_{lower}(Re^E_{lower})^2/(Re^E)^2 = 0.05$ and $a_{LSC}(Re^E_{LSC})^2/(Re^E)^2 = 0.90$, while for the NOB case at $\Delta = 40\,\mathrm{K}$ these fractions are 0.07 and 0.04 for the lower and upper secondary rolls, and the primary LSC contributes 0.89. To visualize these contributions of each subvolume α to the overall change, we show in figure 22 the normalized kinetic energy

deviation $\{a_{NOB,\alpha}(Re^E_{NOB,\alpha})^2 - a_{OB,\alpha}(Re^E_{OB,\alpha})^2\}/(Re^E_{OB})^2$ due to the NOB effect. The upper panel proves that the NOB enhancement of the total kinetic energy is primarily due to the LSC and secondarily to the lower corner roll. For comparison we plotted the corresponding deviations in the lower panel for a hypothetical fluid with thermal expansion coefficient fixed at β_m. Then the enhancement of the LSC contribution is much smaller, while the attenuation and enhancement respectively in the upper and lower secondary rolls are comparable and in addition compensate each other. This leads to the much smaller change in the total kinetic energy in figure 21 as compared with the case when allowing the full temperature dependence of $\beta(T)$ in figure 20. Apparently the *nonlinear* temperature dependence of the buoyancy is very important. Note that the derivative of the buoyancy $\partial\left(g(1-\rho/\rho_m)\right)/\partial T$, corresponding to the driving force per temperature displacement, increases when increasing the temperature deviation $(T - T_m)$ because the coefficient C_2 for the buoyancy expression as reported in Table 1 is positive. Therefore the buoyancy force gets larger and the bulk kinetic energy is more enhanced for given temperature deviation $T - T_c$, if the mean bulk temperature T_c is larger than T_m as observed in figures 2 and 6.

6. Summary and conclusions

In summary, we have studied the temperature profile, the heat current density and the properties of the large scale convections as defined by several representative velocity scales. The centre temperature T_c and the Nusselt number ratio Nu_{NOB}/Nu_{OB} resulting from the two-dimensional numerical NOB simulations are in good agreement with the available experimental data for water (Ahlers *et al.* 2006). Ahlers *et al.* (2006)'s experimental finding $F_\lambda = 1$ for water is argued to be incidental, originating from the specific temperature dependences of the material constants of water at 40 °C. This finding cannot be generalized to other fluids or to other mean temperatures. For water the heat flux reduction due to the deviations from OB conditions is for all practical purposes due to the modified temperature drops over the BLs, represented by F_Δ, whereas for other working fluids it is influenced also by the changes of the thermal BL thicknesses, expressed by F_λ.

The results of the simulations also agree with Ahlers *et al.* (2006)'s predictions for the central temperature, which is based on an extended Prandtl–Blasius theory. As that theory per construction ignores plumes and sidewall effects, these apparently hardly contribute to the determination of the central temperature T_c. However, they do contribute to the shape of the temperature profiles. Our simulations reveal their increasing effect on the profiles with increasing Ra. As the overall heat transfer is determined by the slope of the temperature profiles at the plates, it is to be expected that with increasing Ra the plumes increasingly affect the Nusselt number, in coherence with Grossmann & Lohse (2000, 2001, 2002, 2004)'s unifying theory.

The second part of the paper is devoted to the flow organization in the OB and the NOB cases. First of all, also in the NOB case the large scale convection roll is characterized by only one velocity scale. In contrast, the top and bottom corner flows have different velocity scales in the NOB case, reflecting the enhanced and reduced viscosities close to the respective plates. We defined various different velocity scales, based on global and area averages and peaks in the profiles and analysed how these change under NOB conditions. For the ratio of the energy based Reynolds numbers which also is representative for the others we find $Re^E_{NOB}/Re^E_{OB} \approx (\beta(T_c)/\beta(T_m))^{1/2}$, i.e. NOB deviations in the Reynolds number are strongly governed by the temperature dependence of the thermal expansion coefficient. This finding suggests that fluids

which display no or only a weak temperature dependence of the thermal expansion coefficient hardly show any NOB effects on the Reynolds numbers.

From our point of view the two next steps in numerical work on NOB correction for RB flow are: (i) Study the detailed modifications of the various BL thicknesses and profiles through NOB effects, and (ii) confirm that at least for Prandtl number of 1 and larger the findings of this paper also hold for three-dimensional RB flow. Moreover, NOB experiments focusing on the flow organization, BL layers and Reynolds number modifications would be very desirable.

We thank Guenter Ahlers and Francisco Fontanele Araujo for many fruitful discussions over the last years. The work in Twente is part of the research programme of FOM, which is financially supported by NWO. S. Grossmann acknowledges support by FOM, E. Calzavarini acknowledges support by CNRS.

REFERENCES

Ahlers, G., Brown, E., Fontenele Araujo, F., Funfschilling, D., Grossmann, S. & Lohse, D. 2006 Non-Oberbeck–Boussinesq effects in strongly turbulent Rayleigh–Bénard convection. *J. Fluid Mech.* **569**, 409–445.

Ahlers, G., Calzavarini, E., Fontenele Araujo, F., Funfschilling, D., Grossmann, S., Lohse, D. & Sugiyama, K. 2008 Non-Oberbeck–Boussinesq effects in turbulent thermal convection in ethane close to the critival point. *Phys. Rev.* **E77**, 046302.

Ahlers, G., Fontenele Araujo, F., Funfschilling, D., Grossmann, S. & Lohse, D. 2007 Non-Oberbeck–Boussinesq effects in gaseous Rayleigh–Bénard convection. *Phys. Rev. Lett.* **98**, 054501.

Ahlers, G., Grossmann, S. & Lohse, D. 2009 Heat transfer and large scale dynamics in turbulent Rayleigh–Bénard convection. *Rev. Mod. Phys.* **81**, 503–538.

Amati, G., Koal, K., Massaioli, F., Sreenivasan, K. R. & Verzicco, R. 2005 Turbulent thermal convection at high Rayleigh numbers for a constant-Prandtl-number fluid under Boussinesq conditions. *Phys. Fluids* **17**, 121701.

Amsden, A. A. & Harlow, F. H. 1970 A simplified mac technique for incompressible fluid flow calculations. *J. Comput. Phys.* **6**, 322–325.

Ashkenazi, S. & Steinberg, V. 1999 High Rayleigh number turbulent convection in a gas near the gas–liquid critical point. *Phys. Rev. Lett.* **83**, 3641–3644.

Belmonte, A., Tilgner, A. & Libchaber, A. 1993 Boundary layer length scales in thermal turbulence. *Phys. Rev. Lett.* **70**, 4047–4070.

Belmonte, A., Tilgner, A. & Libchaber, A. 1994 Temperature and velocity boundary layers in turbulent convection. *Phys. Rev.* E **50**, 269–279.

Benzi, R. 2005 Flow reversal in a simple dynamical model of turbulence. *Phys. Rev. Lett.* **95**, 024502.

Boussinesq, J. 1903 *Theorie analytique de la chaleur, vol. 2*. Gauthier-Villars.

Brown, E. & Ahlers, G. 2006 Rotations and cessations of the large-scale circulation in turbulent Rayleigh–Bénard convection. *J. Fluid Mech.* **568**, 351–386.

Brown, E. & Ahlers, G. 2007 Large-scale circulation model for turbulent Rayleigh–Bénard convection. *Phys. Rev. Lett.* **98**, 134501.

Brown, E., Funfschilling, D. & Ahlers, G. 2005 Reorientation of the large-scale circulation in turbulent Rayleigh–Bénard convection. *Phys. Rev. Lett.* **95**, 084503.

Brown, E., Funfschilling, D. & Ahlers, G. 2007 Anomalous Reynolds number scaling in turbulent Rayleigh–Bénard convection. *J. Stat. Mech.* P10005.

Canuto, C., Hussaini, M. Y., Quarteroni, A. & Zang, T. A. 1988 *Spectral Methods in Fluid Dynamics*. Springer.

Chavanne, X., Chilla, F., Castaing, B., Hebral, B., Chabaud, B. & Chaussy, J. 1997 Observation of the ultimate regime in Rayleigh–Bénard convection. *Phys. Rev. Lett.* **79**, 3648–3651.

Chavanne, X., Chilla, F., Chabaud, B., Castaing, B. & Hebral, B. 2001 Turbulent Rayleigh–Bénard convection in gaseous and liquid He. *Phys. Fluids* **13**, 1300–1320.

Ciliberto, S., Cioni, S. & Laroche, C. 1996 Large-scale flow properties of turbulent thermal convection. *Phys. Rev.* E **54**, R5901–R5904.

Ciliberto, S. & Laroche, C. 1999 Random roughness of boundary increases the turbulent convection scaling exponent. *Phys. Rev. Lett.* **82**, 3998–4001.

DeLuca, E. E., Werne, J., Rosner, R. & Cattaneo, F. 1990 Numerical simulations of soft and hard turbulence – preliminary-results for 2-dimensional convection. *Phys. Rev. Lett.* **64**, 2370.

Ferziger, J. H. & Perić, M. 1996 *Computational Methods for Fluid Dynamics*. Springer.

Fontenele Araujo, F., Grossmann, S. & Lohse, D. 2005 Wind reversals in turbulent Rayleigh–Bénard convection. *Phys. Rev. Lett.* **95**, 084502.

Grossmann, S. & Lohse, D. 2000 Scaling in thermal convection: a unifying view. *J. Fluid. Mech.* **407**, 27–56.

Grossmann, S. & Lohse, D. 2001 Thermal convection for large Prandtl number. *Phys. Rev. Lett.* **86**, 3316–3319.

Grossmann, S. & Lohse, D. 2002 Prandtl and Rayleigh number dependence of the Reynolds number in turbulent thermal convection. *Phys. Rev.* E **66**, 016305.

Grossmann, S. & Lohse, D. 2004 Fluctuations in turbulent Rayleigh–Bénard convection: the role of plumes. *Phys. Fluids* **16**, 4462–4472.

Grötzbach, G. 1983 Spatial resolution for direct numerical simulations of Rayleigh–Bénard convection. *J. Comput. Phys.* **49**, 241–264.

Hansen, U., Yuen, D. A. & Kroening, S. E. 1992 Mass and heat-transfer in strongly time-dependent thermal convection at infinite Prandtl number. *Geophys. Astrophys. Fluid Dyn.* **63**, 67–89.

Harlow, F. H. & Welch, J. E. 1965 Numerical calculation of time-dependent viscous incompressible flow of fluid with free surface. *Phys. Fluids* **8**, 2182–2189.

van Heijst, G. J. F., Clercx, H. J. H. & Molenaar, D. 2006 The effects of solid boundaries on confined two-dimensional turbulence. *J. Fluid. Mech.* **554**, 411–431.

Johnston, H. & Doering, C. R. 2009 Rayleigh–Bénard convection with imposed heat flux. *Phys. Rev. Lett.* **102**, 064501.

Kajishima, T., Takiguchi, S., Hamasaki, H. & Miyake, Y. 2001 Turbulence structure of particle-laden flow in a vertical plane channel due to vortex shedding. *JSME Intl J. Ser.* B **44**, 526–535.

Lam, S., Shang, X. D., Zhou, S. Q. & Xia, K.-Q. 2002 Prandtl number dependence of the viscous boundary layer and the Reynolds number in Rayleigh–Bénard convection. *Phys. Rev.* E **65**, 066306.

Lohse, D. & Grossmann, S. 1993 Characteristic scales in Rayleigh–Bénard turbulence. *Phys. Lett.* A **173**, 58–62.

Luijkx, J. & Platten, J. 1981 On the onset of free convection in a rectangular channel. *J. Non-Equilib. Thermodyn.* **6**, 141–158.

Niemela, J., Skrebek, L., Sreenivasan, K. R. & Donnelly, R. 2000 Turbulent convection at very high Rayleigh numbers. *Nature* **404**, 837–840.

Niemela, J., Skrbek, L., Sreenivasan, K. R. & Donnelly, R. J. 2001 The wind in confined thermal turbulence. *J. Fluid Mech.* **449**, 169–178.

Niemela, J. & Sreenivasan, K. R. 2003 Confined turbulent convection. *J. Fluid Mech.* **481**, 355–384.

Oberbeck, A. 1879 über die Wärmeleitung der Flüssigkeiten bei Berücksichtigung der Strömungen infolge von Temperaturdifferenzen. *Ann. Phys. Chem.* **7**, 271.

Peyret, R. & Taylor, T. D. 1983 *Computational Methods for Fluid Flow*. Springer.

Qiu, X. L., Shang, X. D., Tong, P. & Xia, K.-Q. 2004 Velocity oscillations in turbulent Rayleigh–Bénard convection. *Phys. Fluids* **16**, 412–423.

Qiu, X. L. & Xia, K.-Q. 1998 Viscous boundary layers at the sidewall of a convection cell. *Phys. Rev.* E **58**, 486–491.

Roche, P. E., Castaing, B., Chabaud, B. & Hebral, B. 2001 Observation of the 1/2 power law in Rayleigh–Bénard convection. *Phys. Rev.* E **63**, 045303.

Roche, P. E., Castaing, B., Chabaud, B. & Hebral, B. 2002 Prandtl and Rayleigh numbers dependences in Rayleigh–Bénard convection. *Europhys. Lett.* **58**, 693–698.

Schmalzl, J., Breuer, M. & Hansen, U. 2004 On the validity of two-dimensional numerical approaches to time-dependent thermal convection. *Europhys. Lett.* **67**, 390–396.

Shishkina, O. & Wagner, C. 2008 Analysis of sheet-like thermal plumes in turbulent Rayleigh–Bénard convection. *J. Fluid Mech.* **599**, 383–404.

Sreenivasan, K. R., Bershadski, A. & Niemela, J. J. 2002 Mean wind and its reversals in thermal convection. *Phys. Rev.* E **65**, 056306.

Stevens, R., Verzicco, R. & Lohse, D. Radial boundary layer structure and Nusselt number in Rayleigh–Bénard convection. *J. Fluid Mech.* (Submitted)

Stringano, G. & Verzicco, R. 2006 Mean flow structure in thermal convection in a cylindrical cell of aspect-ratio one half. *J. Fluid Mech.* **548**, 1–16.

Sugiyama, K., Calzavarini, E., Grossmann, S. & Lohse, D. 2007 Non-Oberbeck–Boussinesq effects in two-dimensional Rayleigh–Bénard convection in glycerol. *Europhys. Lett.* **80**, 34002.

Sun, C., Xi, H.-D. & Xia, K.-Q. 2005*a* Azimuthal symmetry, flow dynamics, and heat transport in turbulent thermal convection in a cylinder with an aspect ratio of 0.5. *Phys. Rev. Lett.* **95**, 074502.

Sun, C., Xia, K.-Q. & Tong, P. 2005*b* Three-dimensional flow structures and dynamics of turbulent thermal convection in a cylindrical cell. *Phys. Rev.* E **72**, 026302.

Tennekes, H. & Lumley, J. L. 1972 *A First Course in Turbulence*. The MIT Press.

Threlfall, D. C. 1975 Free convection in low-temperature gaseous helium. *J. Fluid Mech.* **67**, 17–28.

Verzicco, R. & Camussi, R. 2003 Numerical experiments on strongly turbulent thermal convection in a slender cylindrical cell. *J. Fluid Mech.* **477**, 19–49.

Werne, J. 1993 Structure of hard-turbulent convection in two-dimensions: numerical evidence. *Phys. Rev.* E **48**, 1020–1035.

Werne, J., DeLuca, E. E., Rosner, R. & Cattaneo, F. 1991 Development of hard-turbulent convection in 2 dimensions – numerical evidence. *Phys. Rev. Lett.* **67**, 3519.

Wu, X. Z. & Libchaber, A. 1991 Non-Boussinesq effects in free thermal convection. *Phys. Rev.* A **43**, 2833–2839.

Xi, H. D., Lam, S. & Xia, K.-Q., From laminar plumes to organized flows: the onset of large-scale circulation in turbulent thermal convection. *J. Fluid Mech.* **503**, 47–56.

Xia, K.-Q., Sun, C. & Zhou, S. Q. 2003 Particle image velocimetry measurement of the velocity field in turbulent thermal convection. *Phys. Rev.* E **68**, 066303.

Xin, Y.-B. & Xia, K.-Q. 1997 Boundary layer length scales in convective turbulence. *Phys. Rev.* E **56**, 3010–3015.

Zhang, J., Childress, S. & Libchaber, A. 1997 Non-Boussinesq effect: thermal convection with broken symmetry. *Phys. Fluids* **9**, 1034–1042.